
Applied Research Laboratory

Technical Report

RADIATION EFFICIENCIES OF A SUBMERGED,
UNBAFFLED FLAT PLATE: NUMERICAL AND
PHYSICAL EXPERIMENTS

by

M. B. Schott

DISTRIBUTION STATEMENT A

Approved for public release
Distribution Unlimited

PENNSTATE



The Pennsylvania State University
APPLIED RESEARCH LABORATORY
P.O. Box 30
State College, PA 16804

**RADIATION EFFICIENCIES OF A SUBMERGED,
UNBAFFLED FLAT PLATE: NUMERICAL AND
PHYSICAL EXPERIMENTS**

by

M. B. Schott

Technical Report No. TR 97-003
May 1997

19970602 133

Supported by:
Naval Surface Warfare Center
Carderock Division
Code 508

L.R. Hettche, Director
Applied Research Laboratory

Approved for public release; distribution unlimited

DTIC QUALITY INSPECTED 1

REPORT DOCUMENTATION PAGE

Form Approved
OMB No. 0704-0188

Public reporting burden for this collection of information is estimated to average 1 hour per response, including the time for reviewing instructions, searching existing data sources, gathering and maintaining the data needed, and completing and reviewing the collection of information. Send comments regarding this burden estimate or any other aspect of this collection of information, including suggestions for reducing this burden, to Washington Headquarters Services, Directorate for Information Operations and Reports, 1215 Jefferson Davis Highway, Suite 1204, Arlington, VA 22202-4302, and to the Office of Management and Budget, Paperwork Reduction Project (0704-0188), Washington, DC 20503.

1. AGENCY USE ONLY (Leave blank)		2. REPORT DATE December 1996	3. REPORT TYPE AND DATES COVERED Master of Science Thesis/Mechanical Eng.	
4. TITLE AND SUBTITLE RADIATION EFFICIENCIES OF A SUBMERGED, UNBAFFLED FLAT PLATE: NUMERICAL AND PHYSICAL EXPERIMENTS			5. FUNDING NUMBERS	
6. AUTHOR(S) M. B. Schott				
7. PERFORMING ORGANIZATION NAME(S) AND ADDRESS(ES) Applied Research Laboratory P.O. Box 30 State College, PA 16804			8. PERFORMING ORGANIZATION REPORT NUMBER 97-003	
9. SPONSORING/MONITORING AGENCY NAME(S) AND ADDRESS(ES) Naval Surface Warfare Center Carderock Division 9500 MacArthur Boulevard West Bethesda, MD 20817-5700 Code 508			10. SPONSORING/MONITORING AGENCY REPORT NUMBER	
11. SUPPLEMENTARY NOTES				
12a. DISTRIBUTION / AVAILABILITY STATEMENT APPROVED FOR PUBLIC RELEASE; DISTRIBUTION UNLIMITED			12b. DISTRIBUTION CODE	
13. ABSTRACT (Maximum 200 words) This thesis presents a method for predicting the radiated sound power of structures that combines numerical models of structural finite element and acoustic boundary element analyses. This method involves the generation and validation of a finite element model of an un baffled, rectangular, flat plate through the use of material properties determined by matching numerical and experimental results and experimentally determined forced response characteristics such as modal frequencies, geometry, damping and generalized force. The finite element model is shown to represent accurately the mode shapes and resonance frequencies of the actual plate. Once a match was achieved between the forced vibration response of the numerical and physical models, the one third octave radiation efficiencies of the finite element model were calculated by means of a lumped acoustic parameter method and compared to experimental measurements conducted in a large water tank. The results of these comparisons show that this approach is capable of predicting the acoustic characteristics of the un baffled, rectangular plate well.				
14. SUBJECT TERMS Structural Acoustics, Finite Element Methods, Boundary Element Methods			15. NUMBER OF PAGES 70	
			16. PRICE CODE	
17. SECURITY CLASSIFICATION OF REPORT UNCLASSIFIED	18. SECURITY CLASSIFICATION OF THIS PAGE UNCLASSIFIED	19. SECURITY CLASSIFICATION OF ABSTRACT UNCLASSIFIED	20. LIMITATION OF ABSTRACT	

ABSTRACT

This thesis presents a method for predicting the radiated sound power of structures that combines numerical models of structural finite element and acoustic boundary element analyses. This method involves the generation and validation of a finite element model of an unbaffled, rectangular, flat plate through the use of material properties determined by matching numerical and experimental results and experimentally determined forced response characteristics such as modal frequencies, geometry, damping and generalized force. The finite element model is shown to represent accurately the mode shapes and resonance frequencies of the actual plate. Once a match was achieved between the forced vibration response of the numerical and physical models, the one third octave radiation efficiencies of the finite element model were calculated by means of a lumped acoustic parameter method and compared to experimental measurements conducted in a large water tank. The results of these comparisons show that this approach is capable of predicting the acoustic characteristics of the unbaffled, rectangular plate well.

TABLE OF CONTENTS

LIST OF FIGURES.....	vi
LIST OF TABLES.....	viii
 CHAPTER 1 INTRODUCTION	 1
1.1 Research Motivation.....	1
1.2 Review of Related Research	2
1.3 Thesis Organization.....	4
 CHAPTER 2 ANALYSIS	 6
2.1 Theoretical Model	6
2.1.1 Classical Plate Theory	6
2.1.2 Acoustic Background	11
2.2 Numerical Model	15
2.2.1 MSC/NASTRAN Plate Model.....	15
2.2.2 Moment Excitation from PZT Actuators	20
 CHAPTER 3 PHYSICAL EXPERIMENTS	 22
3.1 Introduction	22
3.2 Experimental Modal Analysis.....	23
3.3 Experimental Radiation Efficiencies	32
 CHAPTER 4 NUMERICAL EXPERIMENTS	 39
4.1 Introduction.....	39
4.2 Numerical Modal Analysis.....	40
4.3 Numerical Radiation Efficiencies	46
4.3.1 Verification of the Numerical Moment Excitation.....	46
4.3.2 Sound Power Calculations.....	50
 CHAPTER 5 COMPARISON AND DISCUSSION OF MEASURED AND COMPUTER RESULTS.....	 52

CHAPTER 6 CONCLUSIONS AND RECOMMENDATIONS FOR FUTURE WORK.....	65
REFERENCES.....	68

LIST OF FIGURES

Figure 2.1	Plate.....	7
Figure 2.2	Positive state of stress resultants for free edges of a plate.....	10
Figure 2.3	MSC/NASTRAN CQUAD4 element geometry and coordinate systems	16
Figure 2.4	Flow chart of finite element model adjustments to match the physical model of an un baffled, rectangular, flat plate.....	18
Figure 2.5	Half power bandwidth.....	19
Figure 3.1	Schematic of experimental set-up for modal analysis of an un baffled, rectangular, flat plate	27
Figure 3.2	Grid point discretization for location of force hammer impacts on the experimental, flat plate	28
Figure 3.3	Experimentally determined loss factors of a nickel-aluminum-bronze, flat plate	29
Figure 3.4	Experimental (2,1) mode in air, 1490 Hz	30
Figure 3.5	Experimental (4,2) mode in air, 2270 Hz	30
Figure 3.6	Experimental (2,1) mode in water, 1320 Hz	31
Figure 3.7	Experimental (4,0) mode in water, 3280 Hz	31
Figure 3.8	Experimental set-up for the calculation of radiation efficiencies of an un baffled, rectangular, flat plate submerged in water	36
Figure 3.9	Accelerometer locations for experimental radiation efficiency measurements of an un baffled, flat plate	37
Figure 3.10	Experimentally determined transfer function at grid point 117 of an un baffled, rectangular, flat plate.....	38
Figure 4.1	Numerical (0,2) mode in air, 1811 Hz	41

Figure 4.2	Numerical (3,1) mode in air, 2682 Hz	42
Figure 4.3	Numerical (2,0) mode in water, 597 Hz	43
Figure 4.4	Numerical (2,2) mode in water, 2886 Hz	44
Figure 4.5	Location of moment excitation on the physical model of an unbaffled, rectangular, flat plate	48
Figure 4.6	Numerically determined transfer function at grid point 406 of an unbaffled, rectangular, flat plate	49
Figure 5.1	Experimental (1,1) mode, 664 Hz (top) vs. numerical (1,1) mode, 661 Hz (bottom), in air	55
Figure 5.2	Experimental (0,2) mode, 1810 Hz (top) vs. numerical (0,2) mode, 1811 Hz (bottom), in air	56
Figure 5.3	Experimental (2,0) mode, 597 Hz (top) vs. numerical (2,0) mode, 597 Hz (bottom), in water	57
Figure 5.4	Experimental (2,2) mode, 2840 Hz (top) vs. numerical (2,2) mode, 2886 Hz (bottom), in water	58
Figure 5.5	Comparison between experimental and numerical transfer functions of an unbaffled, rectangular, flat plate	61
Figure 5.6	Comparison between experimental and numerical σ of an unbaffled, rectangular, flat plate submerged in water	64

LIST OF TABLES

Table 3.1	Material properties of the physical, unbaffled plate.....	22
Table 3.2	List of equipment for experimental modal analysis of an unbaffled, rectangular, flat plate	23
Table 3.3	Experimental frequencies, mode shapes and loss factors of an unbaffled, rectangular, flat plate	26
Table 3.4	Experimental in-water radiation efficiencies of a nickel-aluminum-bronze, unbaffled, flat plate submerged in water	35
Table 4.1	Material properties of the finite element model of a nickel-aluminum-bronze, flat plate	40
Table 4.2	Numerical in-air and in-water frequencies and mode shapes of an unbaffled, rectangular, flat plate	45
Table 4.3	Frequency dependent moment excitation of the finite element model of an unbaffled, rectangular, flat plate	47
Table 4.4	One third octave frequency bands for sound power calculations of an unbaffled, rectangular, flat plate submerged in water	51
Table 4.5	Numerical radiation efficiencies of an unbaffled, rectangular, flat plate submerged in water	51
Table 5.1	Comparison between calculated and measured mode shapes and natural frequencies for completely free, nickel-aluminum-bronze plate	54
Table 5.2	Comparison between loss factors of nickel-aluminum-bronze plate submerged in water	60
Table 5.3	Comparison between radiation efficiencies of an unbaffled, rectangular, flat plate submerged in water	63

Chapter 1

INTRODUCTION

1.1 Research Motivation

Through the past several decades, the acoustic radiation from flat plates has received considerable attention and investigation, particularly in underwater applications. The focus of these studies has been on the class of radiating panels which are effectively baffled. However, there has been little attention devoted to radiation from unbaffled panels where the fluid on opposite sides of the vibrating surface can interact at the edges. This interaction reduces their radiation efficiencies by converting monopole radiation to dipole radiation at the edges. The goal of this thesis is to determine if a numerical finite element model combined with an acoustic radiation model can be used to predict correctly the acoustic characteristics of an unbaffled structure, since the discontinuities at the boundaries pose formidable computational challenges.

This thesis is an investigation of the radiation efficiency of an unbaffled, rectangular, flat plate submerged in water. We have evaluated a numerical structural acoustic model and compared results from it with experimentally generated data. This model uses a combination of vibration levels derived from a

finite element analysis and acoustic radiation characteristics as predicted by the method of superposition which was developed by Koopmann et. al. [15].

1.2 Review of Related Research

Several different approaches have been used to investigate the sound power radiated from unbaffled, finite plates [1,3,12,24,25]. Of these, there have been relatively few realistic experimental verifications attempted. To the author's knowledge, there are no published studies which predict the sound power from an unbaffled plate using a boundary element acoustic approach.

An iterative technique was developed by Williams [24] and Williams and Maynard [25] which numerically evaluated the acoustic pressure and velocity on and near unbaffled, finite, thin plates vibrating in air. Their technique was based on Rayleigh's integral formula and its inverse. These formulas were written in their angular spectrum form so that a Fast Fourier Transform (FFT) algorithm could be used to evaluate them. The results presented were those of an unbaffled disk; however their solutions suffered from lack of convergence at lower frequencies.

Harbold [12] used non-intrusive velocity measurements to predict acoustic radiation from unbaffled, vibrating plates. He developed an iterative method to predict the acoustic velocity field near the plate surface. To obtain a measure of surface acoustic intensity, a pressure distribution near the plate

surface was assumed and used with the measured velocity field on the plate surface. Using a blocked impedance approach, he assumed a zero velocity field near the plate surface and then they computed the velocity field on the surface of the plate derived from the pressure field over the entire plane of the plate. This was compared to the measured velocity distribution, and like Williams and Maynard, FFT-based equations were used to compute the acoustic pressure and intensity fields.

A theoretical approach to predict the sound power radiated from baffled and unbaffled two-dimensional strips with a prescribed surface motion was determined by Blake [3] through the use of the Wiener-Hopf technique. The Wiener-Hopf technique is used for cases in which the width of the strip is greater than the half-wavelength of the sound in the fluid and for which the wavelength of motion in the strip is smaller than an acoustic wavelength. He compared his theoretical results with experimental measurements to verify that the radiation efficiencies of the unbaffled strips were much less than those of the baffled strips.

Atalla, et. al. [1] predicted the acoustic radiation of an unbaffled, vibrating plate in light fluid. Their method was based on a variational formulation for the plate's displacement and the pressure jump through the structure. A Rayleigh-Ritz approximation with a polynomial set of trial functions was used for the displacement and surface pressures. Their investigation centered on the effect of the baffled vs unbaffled cases and showed that the effect of the baffle is very

important at low frequencies. Their results showed excellent agreement with experiment at low frequencies for a 20.0 X 24.8 X 0.63 inch plate.

In this thesis, we use the method of superposition in which one computes the radiated sound power by dividing the surface of a known vibrating structure into elements and then replacing the vibrating surface with a number of equivalent sources. The basis functions for the numerical analysis are defined as the acoustic fields of discrete simple, dipole and tripole sources. These sources produce the equivalent volume velocity at the surface of the radiator. The velocity distribution over the surface of the body is then represented by a discrete set of volume velocities.

1.3 Thesis Organization

This thesis is divided into six chapters. Chapter one, an introductory chapter, provides an explanation of the motivation for the work and a brief review of related research. Chapter two is devoted to characterizing the theoretical and numerical models of the flat plate and provides background for the method of superposition which was used to predict the radiation efficiencies. In chapter three, a description of the experimental model and typical mechanical responses of the physical plate are given in detail. The fourth chapter describes the numerical experiments and the assumptions made in developing the numerical model. Chapter five gives a detailed comparison between the

experimental model data and the numerical model results. Chapter six concludes the work presented and makes recommendations for applying this method to future studies.

Chapter 2

ANALYSIS

2.1 Theoretical Model

2.1.1 Classical Plate Theory

In the analysis of structures, one frequently encounters structural components for which one dimension, e. g. the thickness h , is much smaller than the other dimensions, as shown in Figure 2.1. This type of structural component is called a plate. We will be primarily concerned with small lateral deflections of such thin plates subjected to lateral loads. The following assumptions are made about the plate: 1) the middle plane of the plate remains unstrained during bending, i. e. it is a neutral surface, 2) the effect of transverse shear strain is negligible, thus normals to the middle surface before deformation remain normal to the same surface after deformation, 3) normal stresses in a direction perpendicular to the plane of the plate are negligible, and 4) the plate material is homogeneous, isotropic, continuous and linearly elastic.

As shown by McFarland [17], the governing partial differential equation defining the lateral deflection of the middle surface of the plate in terms of the applied transverse load is

$$\frac{\partial^4 w}{\partial x^4} + 2 \frac{\partial^4 w}{\partial x^2 \partial y^2} + \frac{\partial^4 w}{\partial y^4} = \frac{p}{D} \quad (2.1)$$

where w is the transverse deflection of the plate, $D = Eh^3/12(1-\nu^2)$, the flexural rigidity, E is Young's modulus, h is the plate thickness, ν is Poisson's ratio, and p is the transverse load.

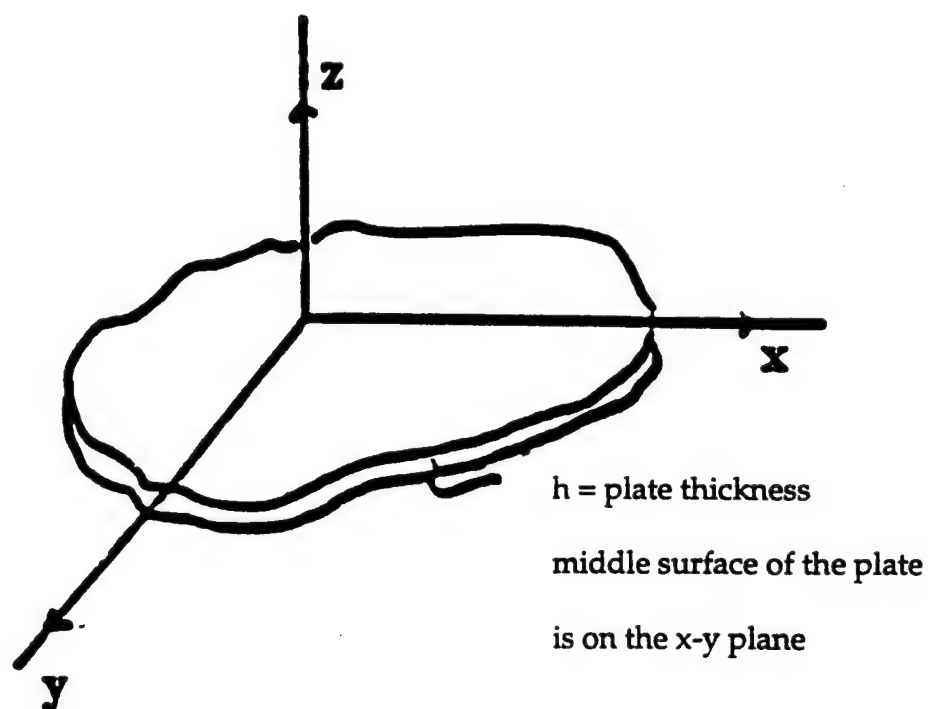


Figure 2.1 Plate

The stress distribution on the transverse faces of the element can be reduced to moments and forces per unit length in the x and y directions. These moments and forces are defined as stress resultants. The moments can be expressed as

$$M_x = -D \left(\frac{\partial^2 w}{\partial x^2} + \nu \frac{\partial^2 w}{\partial y^2} \right) \quad (2.2)$$

$$M_y = -D \left(\nu \frac{\partial^2 w}{\partial x^2} + \frac{\partial^2 w}{\partial y^2} \right) \quad (2.3)$$

Through the addition of equations 2.2 and 2.3, equation 2.1 can be reduced to two second-order partial differential equations

$$M_x + M_y = -D(1 + \nu) \left(\frac{\partial^2 w}{\partial x^2} + \frac{\partial^2 w}{\partial y^2} \right) \quad (2.4)$$

and

$$\nabla^2 M = p \quad (2.5)$$

where $\nabla^2 = \frac{\partial^2}{\partial x^2} + \frac{\partial^2}{\partial y^2}$ and $M = -\frac{M_x + M_y}{1 + \nu}$. If the boundary conditions and the

transverse load p are known, then equation 2.5 can be solved for M(x,y).

Subsequently, equation 2.4 can be solved for w(x,y).

A complete solution of the governing equation 2.1 depends upon the knowledge of the conditions of the plate at its boundaries in terms of the lateral deflection of the middle surface w(x,y). In the most general case, a twisting moment, a bending moment, and a transverse shear force act on each edge of the

plate. An edge on which all three of these stress resultants vanish is defined as a "free edge". Two boundary conditions at each edge are sufficient for a complete solution of the governing equation. The boundary conditions on a free edge parallel to the x-axis at $y=b$ are

$$M_y = -D \left(\nu \frac{\partial^2 w}{\partial x^2} + \frac{\partial^2 w}{\partial y^2} \right)_{y=b} = 0 \quad (2.6)$$

and

$$V_{yz} = -D \left(\nu \frac{\partial^3 w}{\partial y^3} + (2 - \nu) \frac{\partial^3 w}{\partial x^2 \partial y} \right)_{y=b} = 0 \quad (2.7)$$

The boundary conditions on a free edge parallel to the y-axis at $x=a$ are

$$M_x = -D \left(\frac{\partial^2 w}{\partial x^2} + \nu \frac{\partial^2 w}{\partial y^2} \right)_{x=a} = 0 \quad (2.8)$$

and

$$V_{xz} = -D \left(\nu \frac{\partial^3 w}{\partial x^3} + (2 - \nu) \frac{\partial^3 w}{\partial x \partial y^2} \right)_{x=a} = 0 \quad (2.9)$$

A diagram of the stress resultants for a free edge is shown in Figure 2.2.

The solution to the governing differential equation for a completely free plate can be obtained through the method of superposition as shown by Gorman [11]. Gorman superimposed the solutions of four plates each of which has a closed form solution to obtain the solution for the completely free plate. The solution which satisfies the governing differential equation and boundary conditions is

$$W(x, y) = \sum_{m=1}^{k^v} \frac{E_m}{(\beta_m^2 + \gamma_m^2)} \left\{ \frac{\sin \gamma_m y}{\sin \gamma_m} - \frac{\sinh \beta_m y}{\sinh \beta_m} \right\} \cos m\pi x + \quad (2.10)$$

$$\sum_{m=k^v+1}^k \frac{E_m}{(\beta_m^2 - \gamma_m^2)} \left\{ \frac{\sinh \gamma_m y}{\sinh \gamma_m} - \frac{\sinh \beta_m y}{\sinh \beta_m} \right\} \cos m\pi x \quad (2.11)$$

where the first summation pertains to terms for which $\lambda^2 > (m\pi)^2$ and the second summation pertains to terms for which $\lambda^2 < (m\pi)^2$, m represents all positive integers.

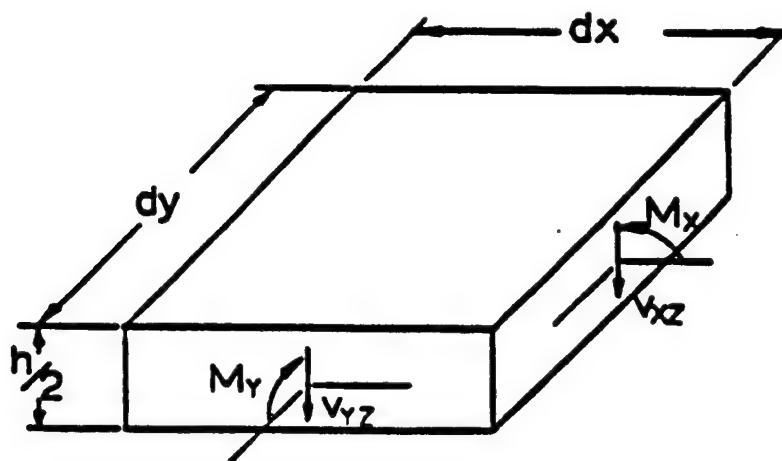


Figure 2.2 Positive state of reduced stress resultants for free edges of a plate

2.1.2 Acoustic Background

In many acoustic applications, the primary quantity used to characterize the noise levels generated by a vibrating structure is the radiated sound power. Radiated sound power is defined as the rate at which energy flows through a surface completely surrounding the structure which includes no other acoustic sources. The normal component of the surface compresses the adjacent fluid causing sound waves to radiate away from the surface.

From an experimental perspective, it is difficult to measure accurately the surface pressure because of the influence of nearby surfaces which scatter the sound waves radiating from the structure. Often the enclosure and measurement devices modify the data. However, it is possible to calculate numerically the acoustic field of a vibrating structure submerged in an infinite fluid medium through the application of the Kirchhoff-Helmholtz equation to the surface pressures. One method for computing acoustic fields numerically based on the principle of wave superposition was used for the numerical predictions in this thesis and will be presented in summary here.

A form of the Kirchhoff-Helmholtz equation can be written as

$$\hat{p}(x) = \frac{-ik\rho c}{4\pi} \iint_S \hat{G}(x/x_s) \hat{v}(x_s) \cdot n_s dS(x_s) \quad (2.12)$$

where $\hat{p}(x)$ represents the pressure at a point in the fluid, ρc is the characteristic acoustic impedance, $\hat{G}(x/x_s)$ is the Green's function representing the acoustic

field due to a source of unit amplitude , and $\hat{v}(x_s) \cdot n$ is the normal velocity of the vibrating structure. Equation 2.12 shows that the acoustic field is dependent only on the surface normal velocity of the vibrating structure and is not a function of the surface pressure. This form of the Kirchhoff-Helmholtz equation is well suited to deriving a lumped parameter model.

The Green's function which is substituted into the Kirchhoff-Helmholtz equation is assumed to satisfy Neumann boundary conditions on the surface of the radiating body which can be written as

$$\nabla_s \hat{G}(x / x_s) \cdot n_s = 0 \quad (2.13)$$

The Neumann condition specifies that the direct radiation from a simple source is scattered by the boundary surface as if the structure were rigid.

The time averaged acoustic power output in terms of the pressure and normal velocity on any surface surrounding the vibrating structure which includes no other acoustic sources can be written as

$$\Pi_w = \frac{1}{2} \iint_s \text{Re} \{ \hat{p}(x) \hat{v}^*(x) \cdot n \} dS(x) \quad (2.14)$$

If the surface in equation 2.14 is assumed to be the boundary surface of the vibrating body, an analytical expression for the power output can then be determined by substituting the pressure field given in equation 2.12 into equation 2.14 and simplifying the result. The time averaged acoustic power output can then be written as

$$\Pi_{av} = \frac{k\rho c}{8\pi} \iint_{S_\mu} \iint_{S_\nu} \text{Im}\{\hat{G}(x_\mu / x_\nu)\} \hat{v}^*(x_\mu) \cdot n_\mu \hat{v}(x_\nu) \cdot n_\nu dS(x_\mu) dS(x_\nu) \quad (2.15)$$

This result is important because it shows that the power output of the vibrating body depends only on the imaginary component of the Green's function which is non-singular.

In a lumped parameter model, the quantities of interest are the average pressure and the volume velocity. One obtains the simplest form of the lumped parameter approximation by assuming that each of the elements vibrates as a piston, such that the surface velocity is constant over each element. The amplitude of the piston vibration is determined by requiring the piston to have the same volume velocity over each element as the specified boundary condition giving equation 2.16.

$$\hat{u}_{piston,\nu} = \frac{1}{S_\nu} \iint_{S_\nu} \hat{v}(x_\nu) \cdot n_\nu dS(x_\nu) \quad (2.16)$$

Substituting this expression into equation 2.15 gives the final result for the lumped parameter approximation for the power output as

$$\Pi_{av} = \frac{1}{2} \sum_{\mu=1}^N \sum_{\nu=1}^N \hat{u}_\mu \hat{u}_\nu \mathfrak{R}_{\mu\nu} \quad (2.17)$$

where

$$\mathfrak{R}_{\mu\nu} = \frac{\mathfrak{R}_0}{S_\mu S_\nu} \iint_{S_\mu} \iint_{S_\nu} \text{Im}\{\hat{G}(x_\mu / x_\nu) / k\} dS(x_\mu) dS(x_\nu) \quad (2.18)$$

and $\mathfrak{R}_0 = k^2 \rho c / 4\pi$.

In the numerical implementation of equation 2.17, the volume velocities of each of the elements are ultimately replaced with basis functions, e.g., monopoles and dipoles that have source strengths equivalent to the volume velocity distributions. Tripole point sources, i.e. the combination of monopoles and dipoles, T_{μ} , with source strengths, s_{μ} , were used as basis functions in this study. The source strengths are related to the volume velocities through the use of equation 2.19

$$\hat{s}_{\mu} = -\frac{ik\rho c}{4\pi} \hat{u}_{\mu} \quad (2.19)$$

The numerical program based on this method is referred to as POWER and can be examined in detail in reference [9]. The expression for the acoustic power used in the lumped parameter superposition method is written as

$$\Pi_{av} = \frac{2\pi}{k\rho c} \sum_{\mu=1}^N \sum_{v=1}^N \text{Re} \{ i\hat{s}_{\mu} \hat{s}_{\nu}^* [T_{\nu}^*(x_{\mu}/x_{\nu}) + i\alpha \nabla_{\mu} T_{\nu}^*(x_{\mu}/x_{\nu}) \cdot n_{\mu}] \} \quad (2.20)$$

where

$$\alpha = \frac{\rho c}{4\pi i \hat{s}_{\mu}} \hat{u}_{\mu} \quad (2.21)$$

The source strengths, s_{μ} , are determined by satisfying the boundary condition using volume velocity matching. The volume velocity matching scheme ensures that the approximate and exact solutions have the same average values over each of the elements. This allows the errors in the approximate solution to equalize as the waves propagate away from the surface of the

radiator. The basis functions, T_{μ} , are the acoustic fields of a tripole source located at the element centroid. The relationship between the volume velocities and the unknown source strengths in matrix form is given by

$$\{s\} = [U]^{-1}\{u\} \quad (2.22)$$

where $[U]$ is

$$U_{\mu\nu} = \frac{1}{ik\rho c} \iint_{s_\nu} \nabla T_\mu(x) \cdot n ds(x) \quad (2.23)$$

In this study, the elemental volume velocities at each grid point, $\{u\}$, are calculated from structural finite element results by integrating the velocity over each element. By operating on $\{u\}$ with $[u]^{-1}$, the source strengths which match the volume velocities over each element are determined. Once these boundary conditions have been satisfied on the surface of the radiator, the acoustic power is calculated via equation 2.20.

2.2 Numerical Model

2.2.1 MSC/NASTRAN Plate Model

The finite element model of the nickel-aluminum-bronze (NAB) plate consisted of 1000 MSC/NASTRAN CQUAD4 elements. The CQUAD4 element was first formulated by I. C. Taig and is described in Zienkiewicz [26]. The important characteristics of the element are that 1) the stresses and strains vary

within the element in a linear manner, 2) the four vertices of the element do not need to be coplanar and 3) the temperature is assumed constant over the element. Gaussian quadrature with a 4×4 grid is used to evaluate the stiffness matrix. The element geometry and coordinate system definitions are shown in Figure 2.3.

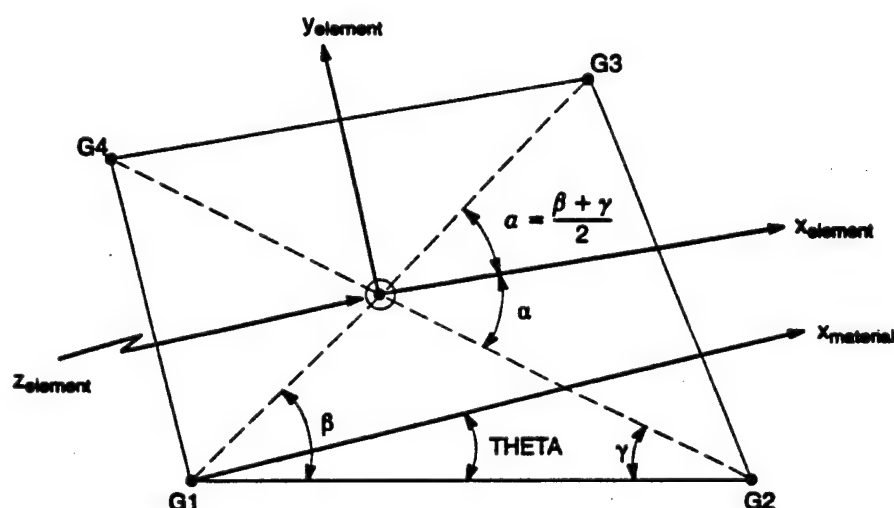


Figure 2.3 MSC/NASTRAN CQUAD4 element geometry and coordinate systems

A finite element model can be used to obtain modal information, e.g. mode shapes and frequencies, as well as dynamic response due to a prescribed forcing function. Figure 2.4 shows how the finite element model of the NAB plate was adjusted to correspond with the physical plate. First, the modal frequencies and geometries were matched, then the forcing function was adjusted.

In a dynamic analysis for lightly damped structures, the bandwidth of the resonant peaks is the range between what is called the half-power points. The half power points are the two points on each side of the resonant peak which have a magnitude equal to $1/\sqrt{2}$ of the value of the resonance peak. Figure 2.5 shows the half-power bandwidth.

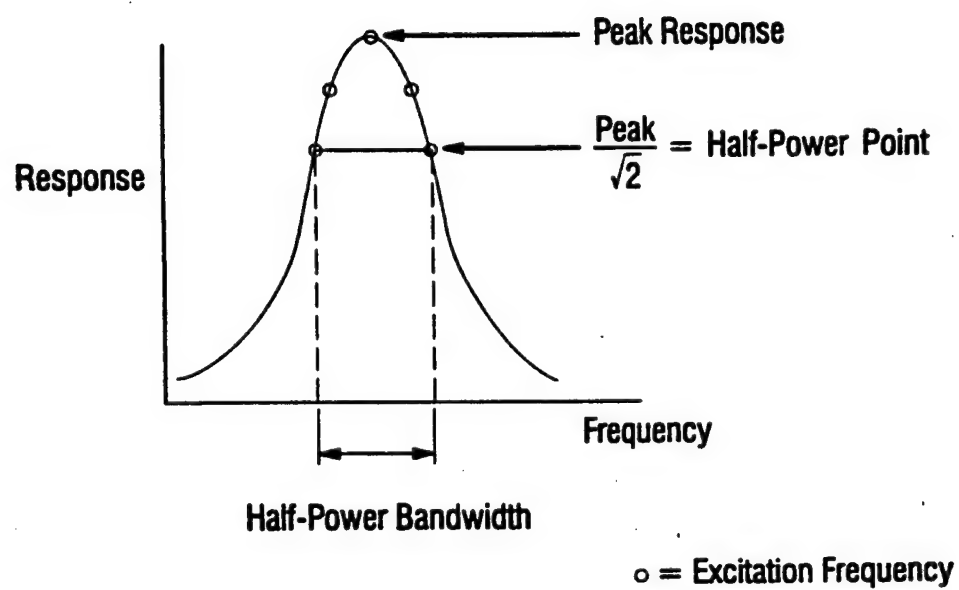


Figure 2.5 Half power bandwidth

2.2.2 Moment Excitation from PZT Actuators

To measure radiation efficiencies in the physical experiments, the NAB plate was excited with 2 PZT Quick Pack™ piezoelectric strain actuators which were mounted on the surface of the plate. Crawley and Luis [6] investigated the use of surface mounted piezoelectric actuators configured as piezoceramic strips. They made the assumption that the piezoelectric actuators could be represented as point forces and moments because the actuator mass was small relative to the total mass of the beam. They also assumed that all resonances of the actuator were higher than the beam's resonance frequencies of interest.

The strains in the piezoelectric were assumed constant throughout its thickness, so that the strain compatibility of the actuator and the substructure was required only at the interface. A sharp rise in the shear stress exists at the end of the piezoelectric, indicating that the strain is transferred between the piezoelectric and the substructure over a small distance near the ends of the actuator. This force, applied at each end of the strip, can be shown as

$$\frac{F}{E_b t_b b} = \frac{1}{(\psi + \alpha)} \left[\frac{\epsilon_b^{s+} + \epsilon_b^{s-}}{2} + \frac{\epsilon_b^{s+} - \epsilon_b^{s-}}{2} \tilde{x} \right] - \left[\frac{1}{\psi + \alpha} \right] \Lambda \quad (2.24)$$

where E_b is the modulus ratio of the beam to the piezoelectric, t_b is the beam thickness, b is the width of the beam, ϵ_b is the strain in the substructure at its left and right ends, \tilde{x} is the nondimensional piezoelectric centered coordinate, ψ is the effective stiffness ratio, α is the substructure equilibrium parameter, and Λ is

the piezoelectric strain ($d_{31}V/t_c$) where d_{31} is the piezoelectric constant and t_c is the thickness of the piezoelectric. If bending is being excited, the moment applied to the beam by these forces is equal to $M_0 = Ft_b$. This shows that surface bonded piezoelectric actuators can be modeled as generating a moment at the ends of the PZT strips.

Chapter 3

PHYSICAL EXPERIMENTS

3.1 Introduction

This chapter describes the physical model of the plate used in the experiment and explains the procedure for measuring its resonance frequencies, mode shapes and calculating its radiation efficiencies in one-third octave bands. The plate itself was a 10 X 16 X 1.1 inch rectangular, flat plate made from a nickel-aluminum-bronze (NAB) alloy. The physical properties of the plate are shown in Table 3.1.

Table 3.1 Material properties of the physical, unbaffled plate

Young's modulus	16.0×10^6 psi
Poisson's ratio	0.32
density	0.276 lb/in ³

3.2 Experimental Modal Analysis

A modal analysis in air and in water was performed on the plate to determine its modal frequencies, mode shapes, and damping for comparison and validation of the finite element model. A schematic of the experimental apparatus for determining the vibration response and modal characteristics of the plate is shown in Figure 3.1. Each individual component is listed in Table 3.2.

Table 3.2 List of equipment for experimental modal analysis of an unbaffled, rectangular, flat plate

Facility	ARL Reverberant Water Tank
Model Type	NAB flat plate
Accelerometers	PCB Model #W353
Force Hammer	PCB Model #7612
ICP Signal Conditioner	PCB 12-channel Model #483B07
Spectrum Analyzer	Spectral Dynamics SD380
Computer	Gateway 486DX PC
Analysis Software	SMS Starmodal, version 4.0

The plate was suspended from a crane by wires connected to screw-eyes on one end of the plate in order to simulate a free boundary condition on all four sides. The surface of the plate was discretized into an 11 by 17 grid for a total of 187 grid points as shown in Figure 3.2. The plate was excited by a waterproof PCB force hammer with a plastic tip. The plastic tip was chosen to provide a unit impulse power spectrum with a spectral roll-off over a frequency span of 0-4000 Hz. This ensured that enough energy was imparted to the system at low frequency while maintaining an adequate signal to noise ratio at 4000 Hz.

The plate response was measured using a PCB W353 accelerometer. The modal testing was accomplished by using the method of reciprocity. The acceleration response of the structure was measured with a fixed accelerometer while each of the 187 grid points was excited with the roving force hammer. Transfer functions for each grid point were recorded in 5 Hz increments and processed by the SD380 spectrum analyzer in 5 Hz increments from 0 to 4000 Hz. Five impacts per grid point were used to calculate a root mean square average of the frequency response function (FRF). Each FRF measurement was transferred to Star Modal (a modal analysis software package) via IEEE interface from the spectrum analyzer.

Once the transfer functions were obtained, the resonance frequencies for the plate were determined by examining the average transfer functions in Star Modal [22]. Narrow bands were selected to include the peaks of all of the

resonance frequencies. A rational fraction polynomial curve fit was determined within each selected band. Each fitted band was then incorporated into a complex, "synthesized" FRF. The poles of the complex FRF contained the modal loss factors and resonance frequencies while the residues provided the modal amplitudes. Figure 3.3 shows the experimentally determined loss factors. The modal parameters were then calculated which allowed mode shapes for each selected resonance frequency to be obtained. This procedure was repeated for the plate's in-water modes as well. Table 3.3 lists the resonance frequencies, mode shapes and loss factors for both the in-air and in-water experiments. Figures 3.4 to 3.6 show some representative mode shapes of the structure both in-air and in-water.

Table 3.3 Experimental resonance frequencies, modes shapes and loss factors of an unbaffled, rectangular, flat plate

mode number	mode(i,j)	in-air frequency	in-air loss factor	in-water frequency	in-water loss factor
1	(1,1)	664 Hz	$\ll 1$		0.01
2	(2,0)	697 Hz	-0.0444	597 Hz	0.01
3	(2,1)	1490 Hz	-0.0007	1320 Hz	0.01
4	(0,2)	1810 Hz	0.0017	1610 Hz	0.02
5					
6	(1,2)	2270 Hz	0.0012		
7	(3,1)	2680 Hz	0.0014		
8	(2,2)	3130 Hz	0.0013	2840 Hz	$\ll 1$
9	(4,0)	3680 Hz	0.0009	3280 Hz	$\ll 1$

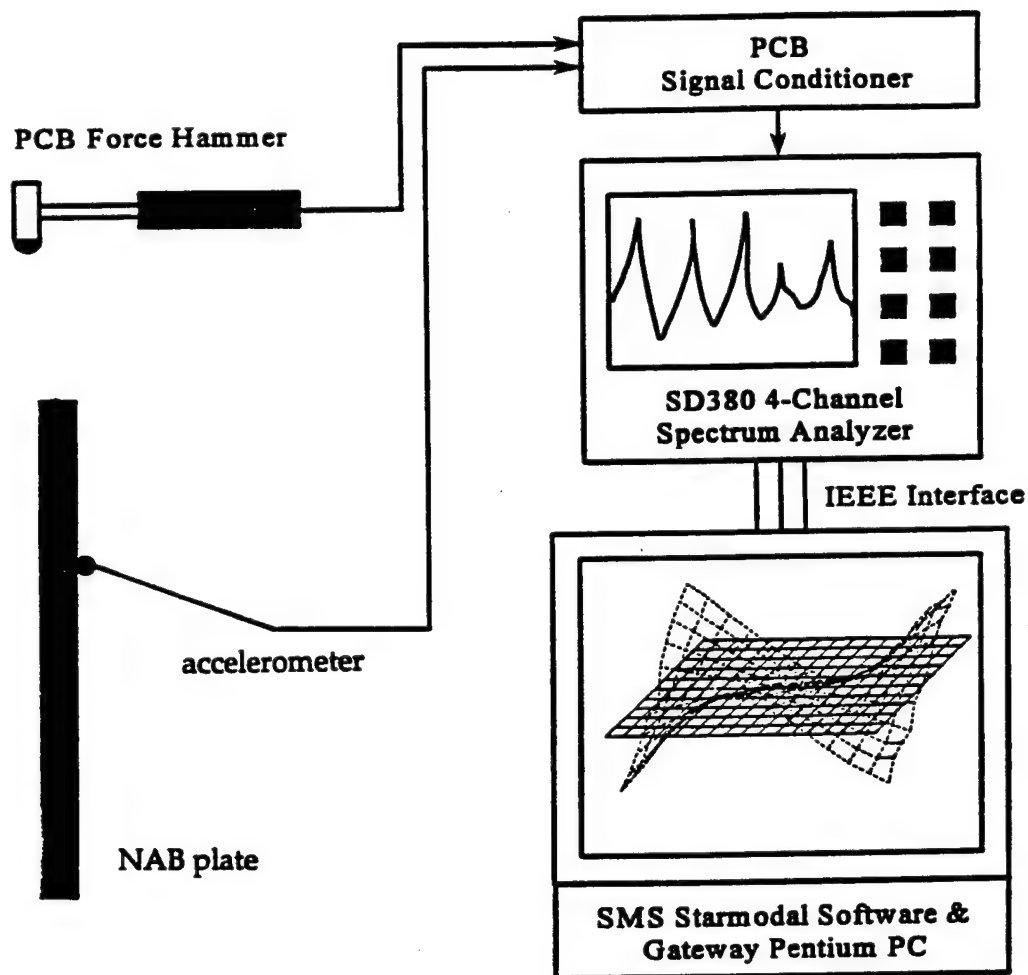


Figure 3.1 Schematic of experimental set-up for modal analysis of an un baffled, rectangular, flat plate

1	12	23	34	45	56	67	78	89	100	111	122	133	144	155	166	177
2	13	24	35	46	57	68	79	90	101	112	123	134	145	156	167	178
3	14	25	36	47	58	69	80	91	102	113	124	135	146	157	168	179
4	15	26	37	48	59	70	81	92	103	114	125	136	147	158	169	180
5	16	27	38	49	60	71	82	93	104	115	126	137	148	159	170	181
6	17	28	39	50	61	72	83	94	105	116	127	138	149	160	171	182
7	18	29	40	51	62	73	84	95	106	117	128	139	150	161	172	183
8	19	30	41	52	63	74	85	96	107	118	129	140	151	162	173	184
9	20	31	42	53	64	75	86	97	108	119	130	141	152	163	174	185
10	21	32	43	54	65	76	87	98	109	120	131	142	153	164	175	186
11	22	33	44	55	66	77	88	99	110	121	132	143	154	165	176	187

Figure 3.2 Grid point discretization for location of force hammer impacts on the experimental, flat plate

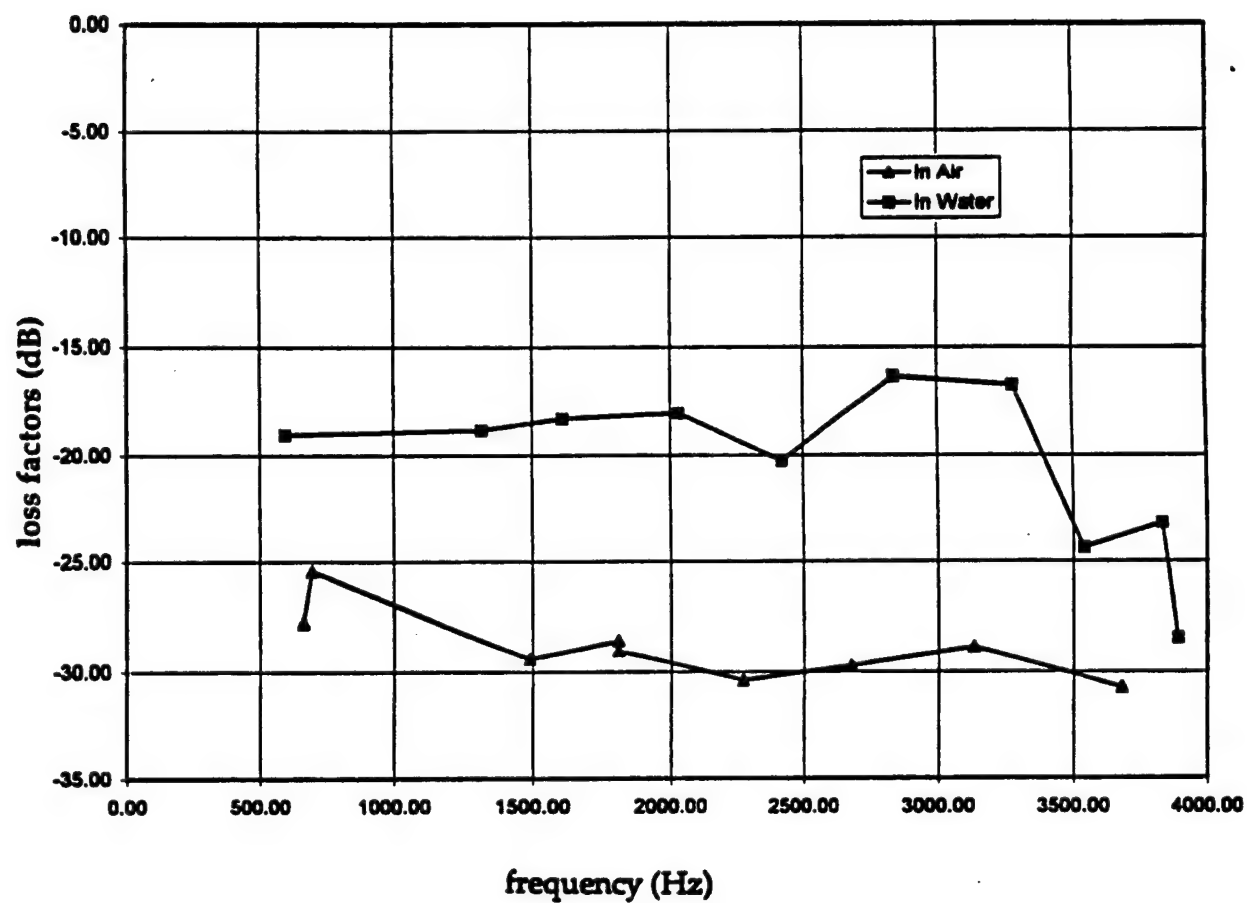


Figure 3.3 Experimentally-determined loss factors of a nickel-aluminum-bronze, flat plate

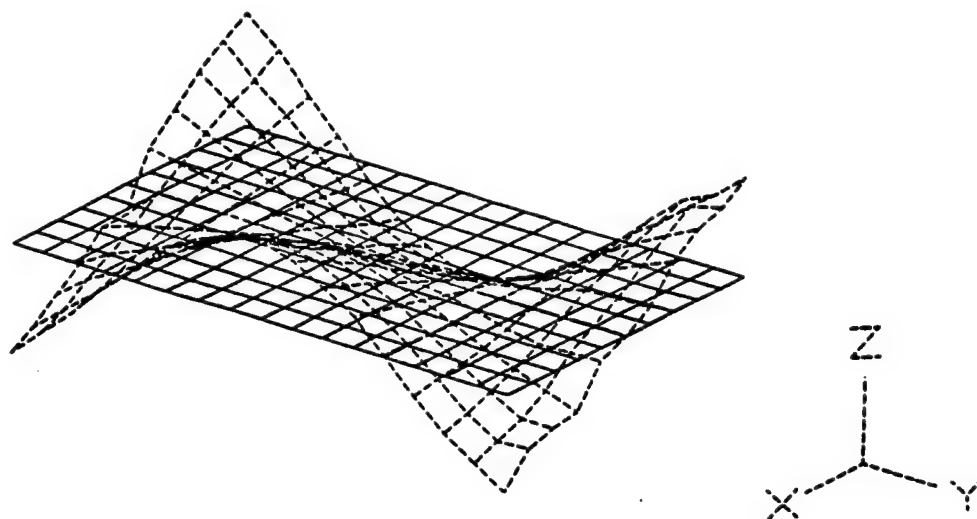


Figure 3.4 Experimental (2,1) mode in air, 1490 Hz

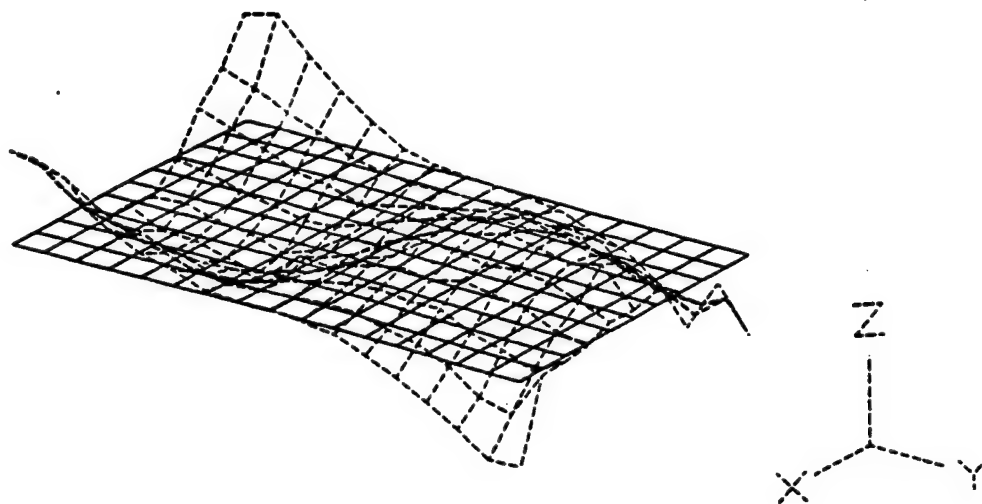


Figure 3.5 Experimental (1,2) mode in air, 2270 Hz

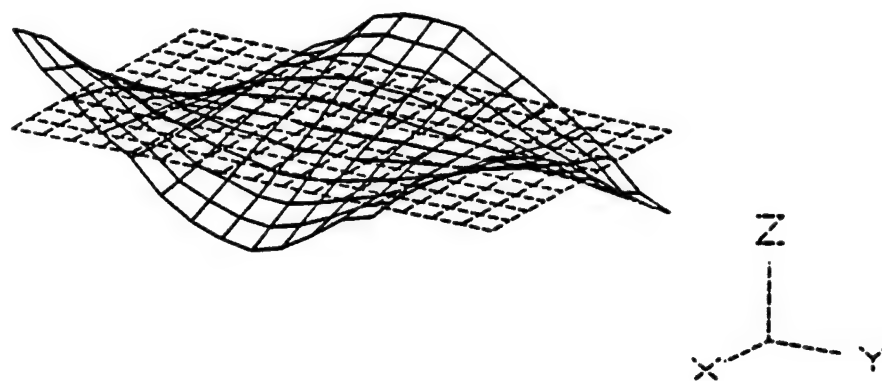


Figure 3.6 Experimental (2,1) mode in water, 1320 Hz

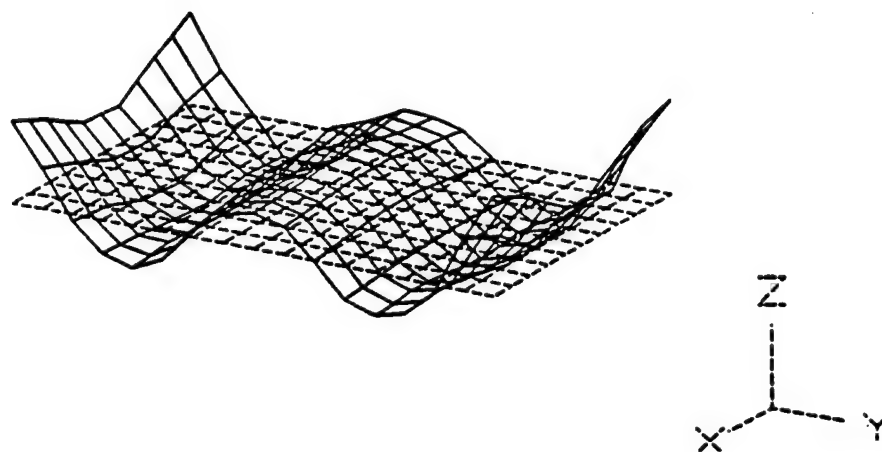


Figure 3.7 Experimental (4,0) mode in water, 3280 Hz

3.2 Experimental Radiation Efficiencies

Radiation efficiency as defined by Fahy [10] is

$$\sigma = \frac{\Pi}{\rho c_0 S \langle v^2 \rangle} \quad (3.1)$$

where Π defines the power radiated by the object, ρ is the density of the fluid, c_0 is the speed of sound in the fluid, S represents the surface area of the radiating object and $\langle v^2 \rangle$ designates the mean of the velocity squared, averaged over the radiating surface of the object.

In practice, the radiation efficiency can be measured in a reverberant room (or water tank) using experimental techniques presented by Cremer, Heckl and Ungar [7] and Blake [3] and used by Weyer and Szwerc [23].

When measured in a reverberant room, the radiation efficiency is determined using

$$\sigma_R = \rho_0 c_0 f^2 R(f) \frac{1}{A_p} \frac{\Phi_{pp}(f)}{\Phi_{aa}(f)} \quad (3.2)$$

where f is the frequency of interest, $R(f)$ the frequency dependent room constant, A_p the radiating area of the structure, $\Phi_{pp}(f)$ the average sound pressure level in the room and $\Phi_{aa}(f)$ the surface averaged acceleration of the structure.

The room constant, or sound absorption of a room is defined by Kinsler et. al. [13] as :

$$R(f) = \frac{55.2V}{c_0 T_r} \quad (3.3)$$

where V is the volume of the room in m^3 and T_r the reverberation time in seconds. The reverberation time is the time required for the sound pressure level in the room to drop 60 dB following the removal of a continuous sound source. The reverberation time is a function of the room surface area and the absorption of the room surfaces. Given the reverberation times, the radiation efficiency for the flat plate could be computed after the vibration and pressure fields were measured.

The vibration field of the plate was determined using 15 accelerometer locations and the resulting pressure field in the reverberant tank was typically sampled at 3 to 5 locations using hydrophones. Figure 3.8 shows the experimental set-up for the measurement of radiation efficiencies. Accelerometer and hydrophone data were combined to compute an overall radiation efficiency for the plate using equation 3.2. Figure 3.9 shows the first group of fifteen accelerometer locations for the plate. These accelerometers were then removed and placed on the next fifteen grid point locations. The plate was excited using 2 PZT Quick Pack™ strain actuators and a Quick Pack™ Power Amplifier.

Before each run, the user of the data acquisition program specified the radiating area of the structure, the number of accelerometers and the number of hydrophones. At the end of each run, accelerometer, hydrophone and voltage/acceleration transfer function drive levels were gathered using LABVIEW [16]. LABVIEW was used to control the HP3561A analyzer via the

IEEE bus and to calculate the radiation efficiencies by the use of equation 3.2.

Data were acquired in one third octave bands and the results were transferred from the analyzer to the control computer. Results stored for each run consisted of gains, sensitivities, the radiating area of the test object, individual accelerometer and hydrophone spectra, voltage/acceleration transfer functions of drive levels and a computed radiation efficiency. After specifying the correct transducer sensitivities and gains, the stored spectra were in engineering units. Figure 3.10 shows an example of one of the actuator voltage/acceleration vs. frequency transfer functions collected which was converted to velocity vs. frequency. The experimentally determined radiation efficiencies are shown in Table 3.4.

**Table 3.4 Experimental radiation efficiencies of a nickel-aluminum-bronze
unbaffled, flat plate submerged in water**

Frequency (Hz)	Radiation Efficiency (dB)
2000	-28
2500	-27
3150	-27
4000	-18
5000	-5
6300	-13
8000	-14
10000	-14

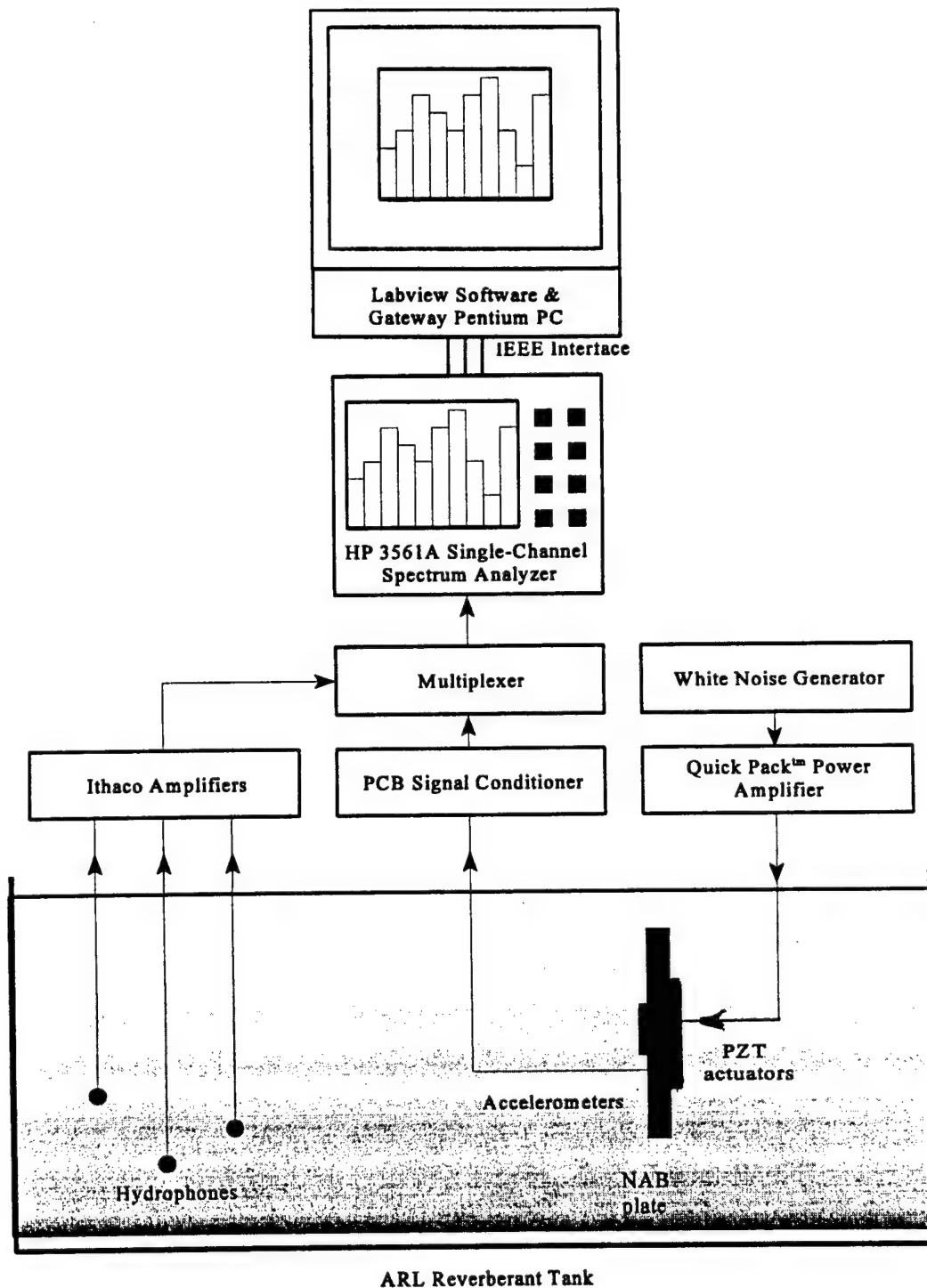


Figure 3.8 Experimental set-up for the calculation of radiation efficiencies of an unbaffled, rectangular, flat plate submerged in water

1	12	23	34	45	56	67	78	89	100	111	122	133	144	155	166	177
2	13	24	35	46	57	68	79	90	101	112	123	134	145	156	167	178
3	14	25	36	47	58	69	80	91	102	113	124	135	146	157	168	179
4	15	26	37	48	59	70	81	92	103	114	125	136	147	158	169	180
5	16	27	38	49	60	71	82	93	104	115	126	137	148	159	170	181
6	17	28	39	50	61	72	83	94	105	116	127	138	149	160	171	182
7	18	29	40	51	62	73	84	95	106	117	128	139	150	161	172	183
8	19	30	41	52	63	74	85	96	107	118	129	140	151	162	173	184
9	20	31	42	53	64	75	86	97	108	119	130	141	152	163	174	185
10	21	32	43	54	65	76	87	98	109	120	131	142	153	164	175	186
11	22	33	44	55	66	77	88	99	110	121	132	143	154	165	176	187

Figure 3.9 Accelerometer locations for experimental radiation efficiency measurements of an unbaffled, flat plate

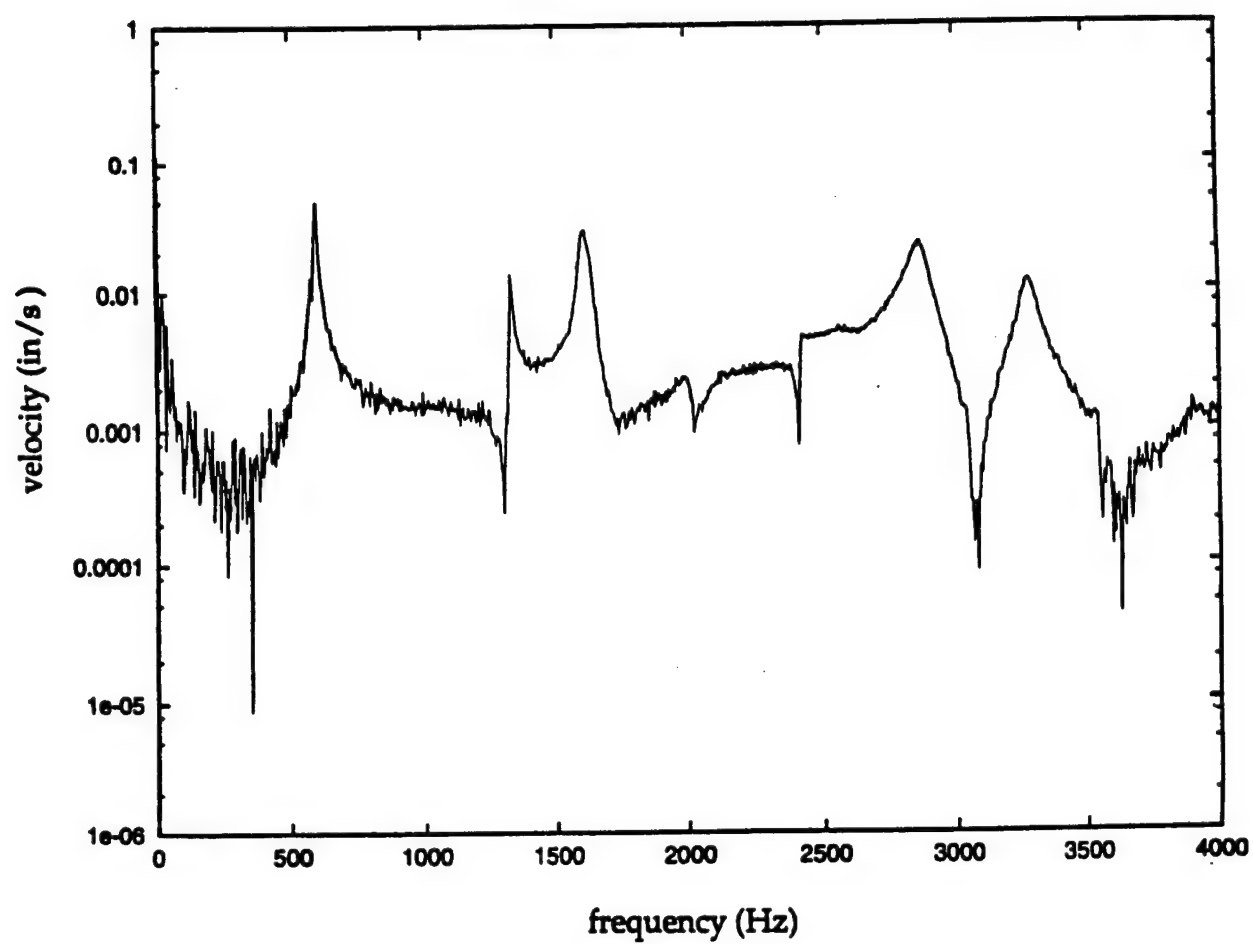


Figure 3.10 Experimentally determined transfer function at grid point 117 of an unbauffed, rectangular, flat plate

Chapter 4

NUMERICAL EXPERIMENTS

4.1 Introduction

This chapter describes the numerical model of the flat plate and explains the method for implementing the experimentally determined characteristics of the plate into the finite element model. A finite element model of the plate was generated in MSC/XL [20] by discretizing the face of the 10 x 16 x 1.1 inch plate into a grid of 25 by 40, two-dimensional quadrilateral elements. This mesh refinement was chosen based on MSC/NASTRAN's recommendation of eight to ten elements per half wave for dynamic analysis. This is to ensure that at the frequencies of interest, the mesh density captures the behavior of the structure accurately.

The element selected was the MSC/NASTRAN CQUAD4. This is an isoparametric, membrane-bending element. The material properties of the finite element model are as shown in Table 4.1.

Table 4.1 Material properties of the finite element model of a nickel-aluminum-bronze, flat plate

Young's Modulus	17.55×10^6 psi
Poisson's ratio	0.32
density	0.276 lb/in ³

4.2 Numerical Modal Analysis

The usual first step in performing a dynamic analysis is to determine the resonance frequencies and mode shapes of the structure. These results characterize the basic dynamic behavior of the structure and are an indication of how the structure will respond to dynamic loading. Computation of the resonance frequencies and mode shapes is performed by solving an eigenvalue problem. The description of the MSC/NASTRAN eigensolution method is given in detail in reference [18].

Free edge boundary conditions were imposed on the structure and a modal analysis in air and in water was performed. This analysis determined the plate's eigenvalues (resonance frequencies) and eigenvectors (mode shapes) for comparison with the experimental resonance frequencies and mode shapes. A list of the resonance frequencies and mode shapes is given in Table 4.2. The in-

water finite element model made use of MSC/NASTRAN's virtual fluid mass capability. The fluid is represented by a coupled mass matrix which is attached directly to the structural points. Both sides of the plate were defined as wetted structural elements. Figures 4.1 to 4.4 show representative mode shapes of the structure.

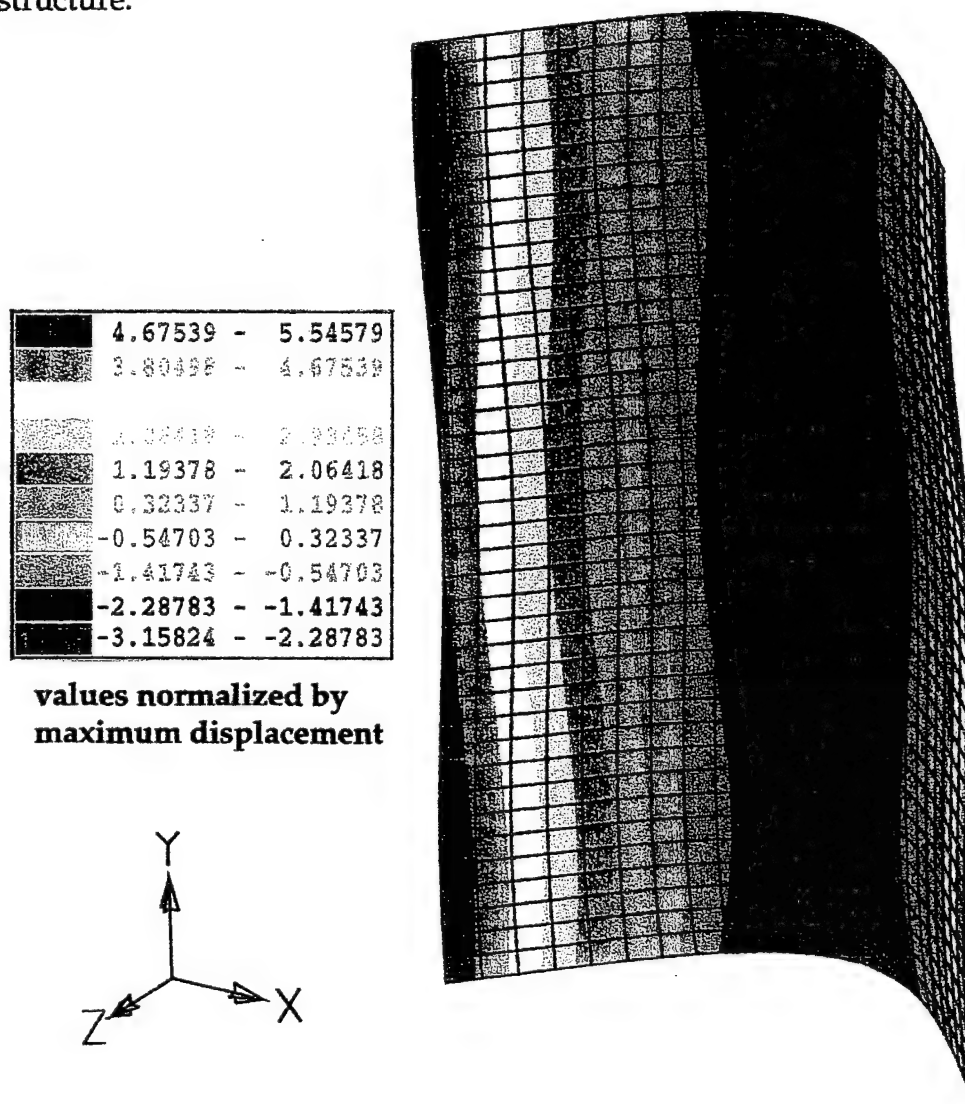


Figure 4.1 Numerical (0,2) mode in air, 1811 Hz

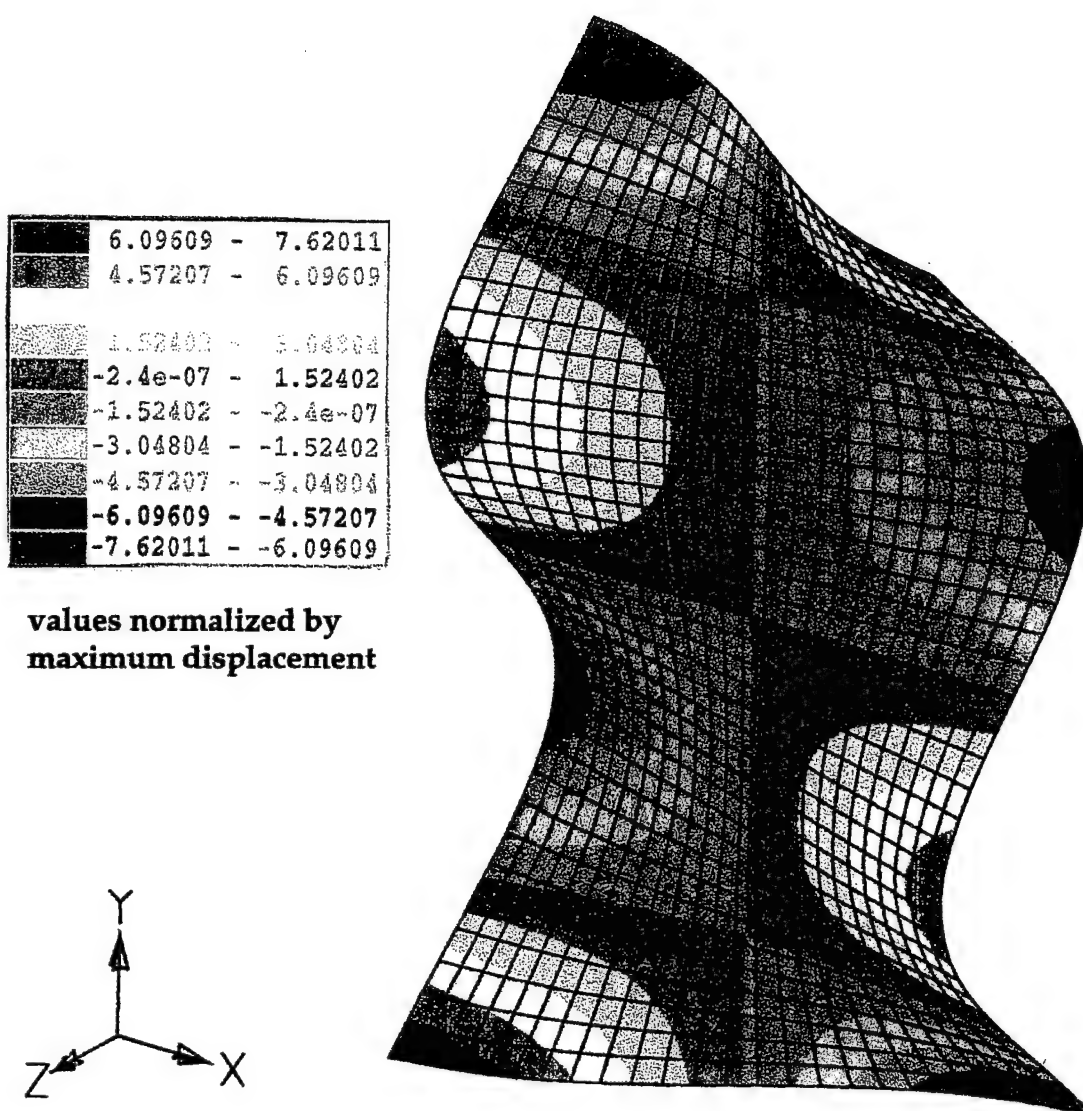


Figure 4.2 Numerical (3,1) mode in air, 2682 Hz

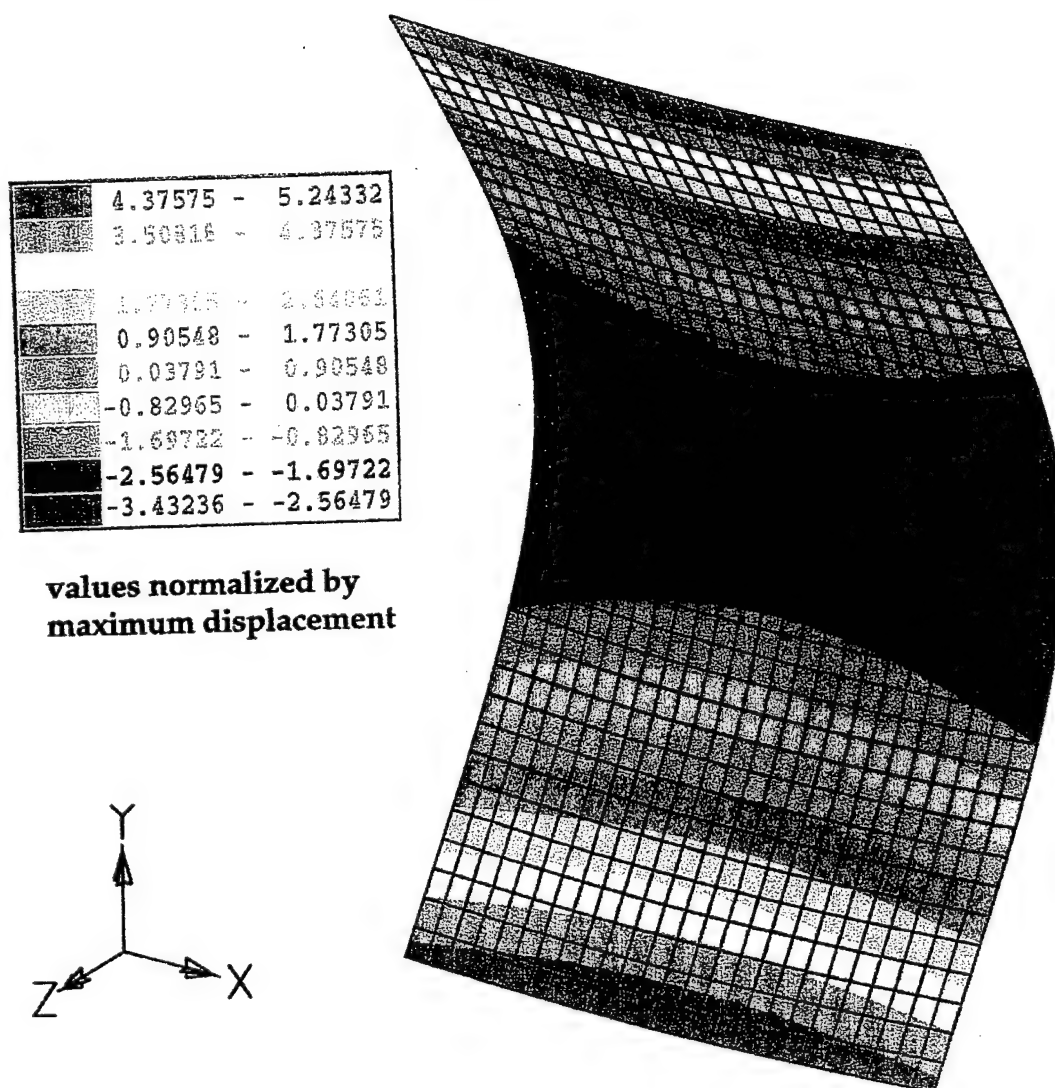


Figure 4.3 Numerical (2,0) mode in water, 597 Hz

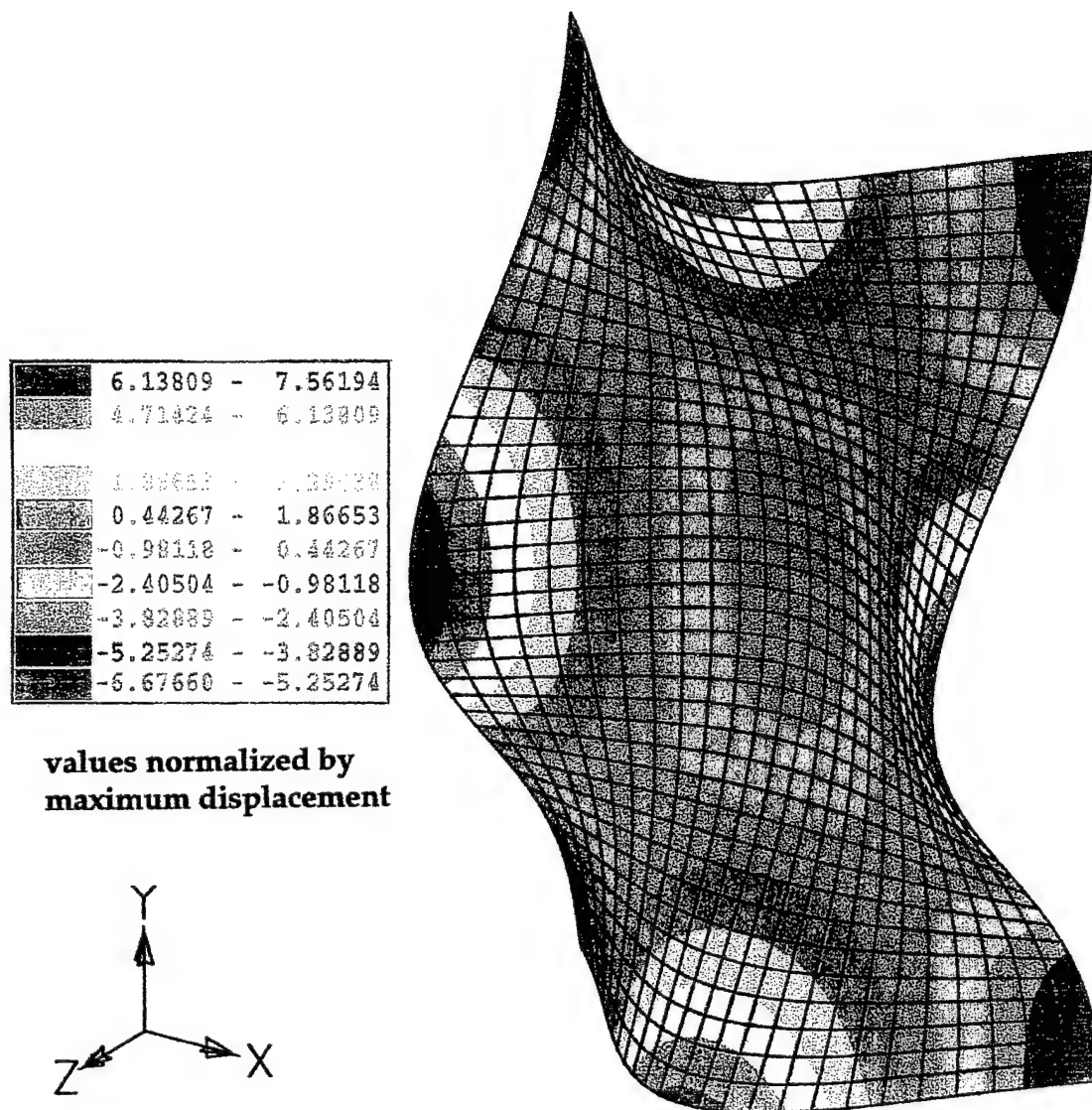


Figure 4.4 Numerical (2,2) mode in water, 2886 Hz

Table 4.2 Numerical in-air and in-water frequencies and modes shapes of an unbaffled, rectangular, flat plate

mode number	mode(i,j)	in-air frequency (Hz)	in-water frequency (Hz)
1	(1,1)	661	584
2	(2,0)	690	597
3	(2,1)	1491	1333
4	(0,2)	1811	1611
5	(3,2)	1847	1642
6	(1,2)	2265	2021
7	(3,1)	268	2428
8	(2,2)	3173	2886
9	(4,0)	3504	3300

4.3 Numerical Radiation Efficiencies

4.3.1 Verification of the Numerical Moment Excitation

In the physical experiments, the plate was excited using two surface bonded piezoelectric actuators as described in Chapter two. Before numerical sound power calculations could be performed, the correct moment excitation of the plate needed to be determined for application to the dynamic model.

First, a small sample of transfer functions from the experimental data were converted from voltage/acceleration to velocity through the use of equation 4.1.

$$\dot{X} = \text{magnitude} \times \frac{1g}{0.1\text{volt}} \times \frac{(32.2 \frac{ft}{s^2})(12 \frac{in}{ft})}{g} \times \frac{1}{2\pi f} \quad (4.1)$$

Figure 4.5 shows how the moments are generated on the actual plate. These moments were applied on the finite element model at four grid points which corresponded with the location of the ends of the PZT strips on the physical plate. Using these moments as the forcing function, a frequency response analysis was conducted. Velocity output was requested at a grid point which corresponded with the same location on the experimental model for frequencies between 0 Hz and 4000 Hz. The numerical and corresponding experimental transfer functions were plotted. Frequency dependent damping was incorporated into the model so that the amplitudes of the resonant peaks of the

experimental and numerical transfer functions agreed as closely as possible. This process was repeated while alternately adjusting the moment excitation and damping until acceptable values for each of these were achieved. The experimental transfer functions were recorded only in the 0 to 4000 Hz range, so assumptions were made for the moment excitation values above 4000 Hz. Values of 15 in-lb were assumed for the moment excitation at higher frequencies for use in the sound power calculations. The values of the calculated moments in each frequency range are listed in Table 4.3. Figure 4.6 is a plot of the numerically generated velocity vs. frequency transfer function up to 4000 Hz.

Table 4.3 Frequency dependent moment excitation of the finite element model of an un baffled, rectangular, flat plate

frequency range (Hz)	moment (in-lb)
0 to 1000	15
1000 to 2150	5
2150 to 4000	25

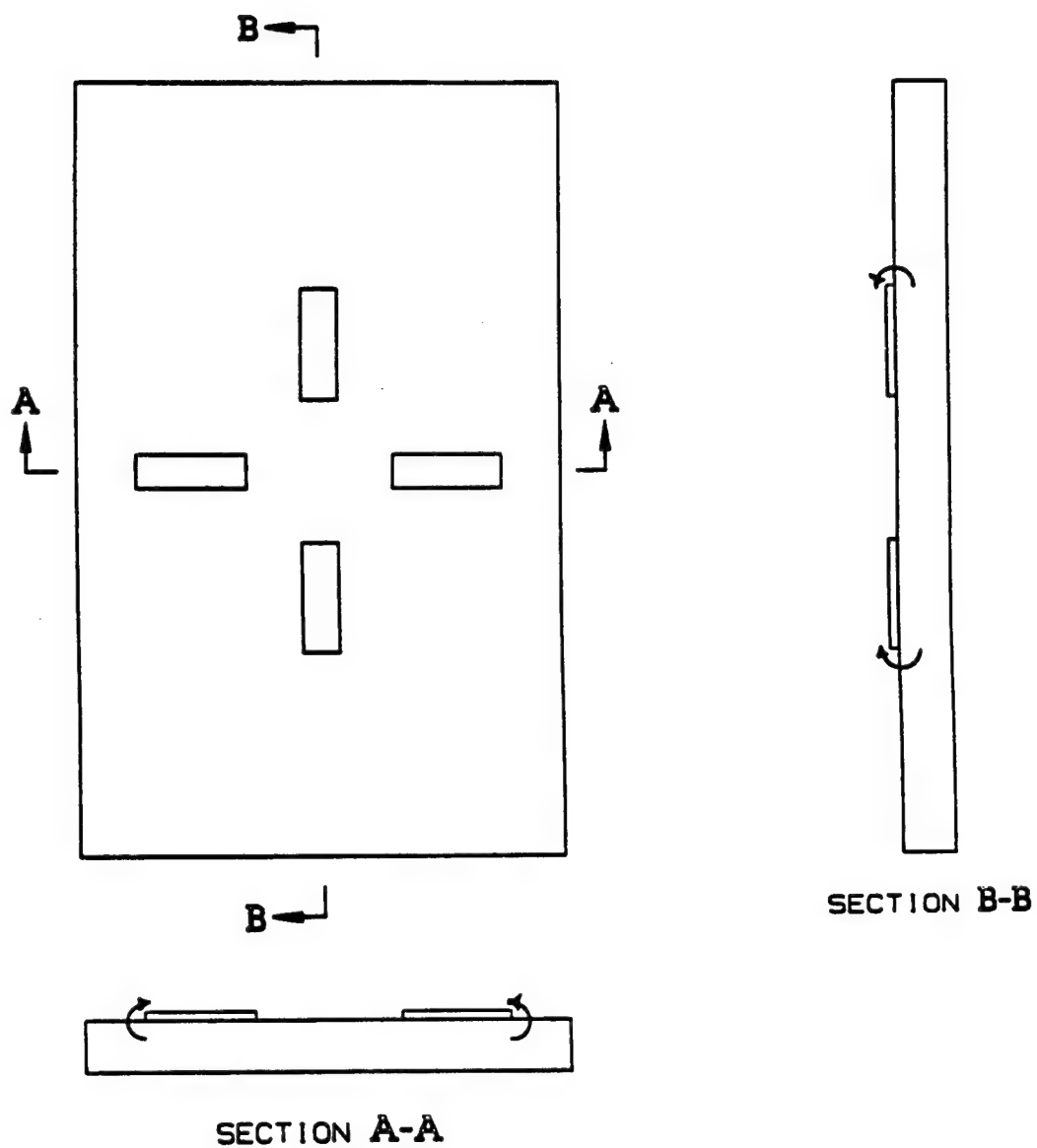


Figure 4.5 Location of moment excitation on the physical model of an unbaffled, rectangular, flat plate

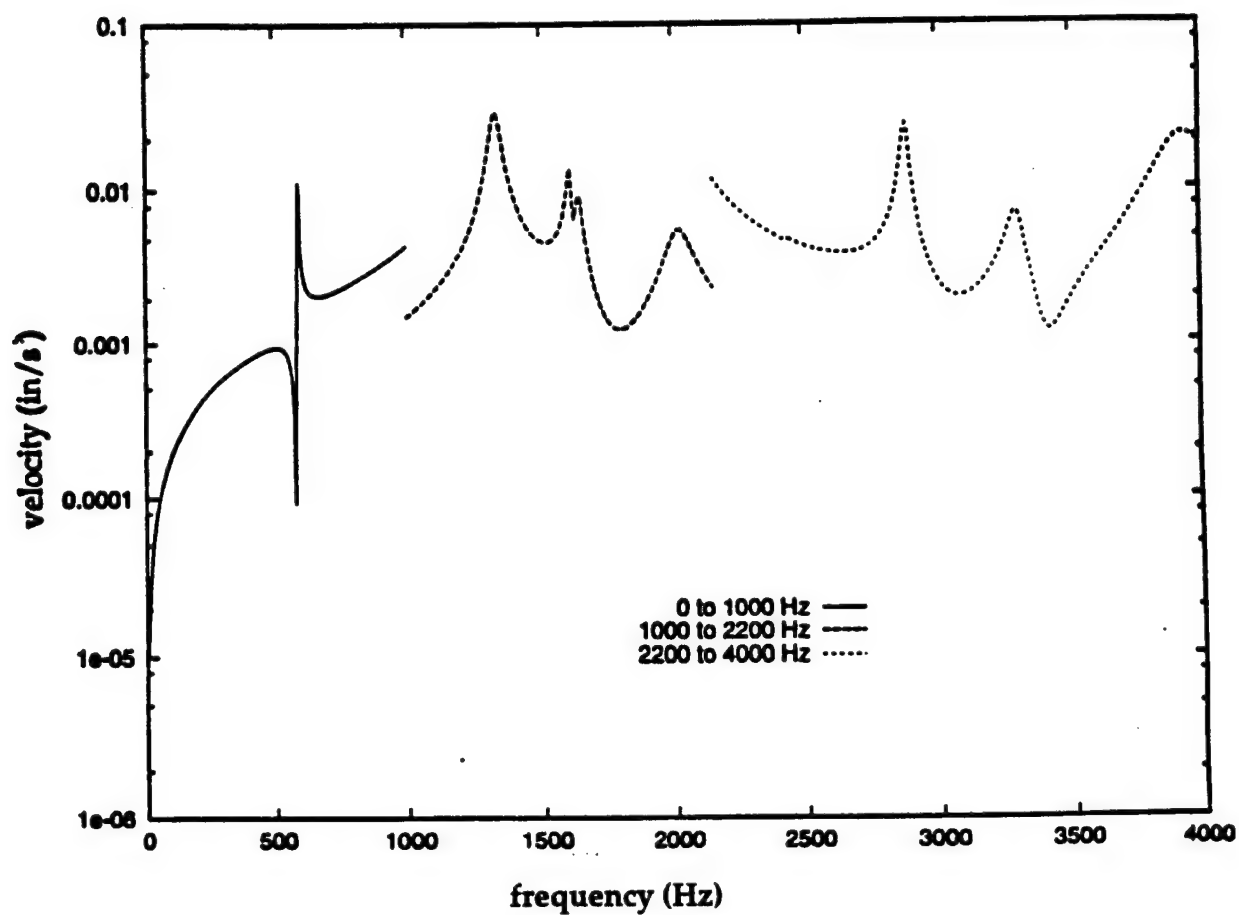


Figure 4.6 Numerically determined transfer function at grid point 406 of an unbaffled, rectangular, flat plate

4.3.2 Sound Power Calculations

Frequency response analysis is a method used to compute structural response to steady-state oscillatory excitation. Before sound power calculations could be performed on the structure, a frequency response analysis needed to be carried out to extract the displacements (volume velocities) of the plate. The finite element model incorporated the half-power points as described in Chapter two into each frequency response analysis. The excitation was the frequency dependent moment determined from measurements as described in Chapter five.. These moment excitations were used in three separate frequency response analyses: from 1000 Hz to 2150 Hz, from 2150 Hz to 4000 Hz and from 4000 Hz to 10000 Hz.

The volume velocities computed from displacements from each frequency response analysis were used as input to the POWER code. These displacements at each resonance frequency as well as the two half power points on each side of the resonance frequency were requested. The radiated sound power output was divided into one third octave frequency bands as shown in Table 4.4. After the completion of all three analyses, the power output in watts was then averaged for each of the eight one third octave center frequencies. Radiation efficiencies were then calculated through the use of equation 3.1 and converted to decibels. Table 4.5 lists the numerical radiation efficiencies for each one-third octave band from 2 to 8 KHz.

Table 4.4 One third octave frequency bands for sound power calculations of an unbaffled, rectangular, flat plate submerged in water

lower band limit (Hz)	center frequency (Hz)	upper band limit (Hz)
1788	2000	2239
2239	2500	2818
2818	3150	3548
3548	4000	4467
4467	5000	5623
5623	6300	7079
7079	8000	8913

Table 4.5 Numerical radiation efficiencies of an unbaffled, rectangular, flat plate submerged in water

center frequency (Hz)	radiation efficiency (dB)
2000	-32
2500	-26
3150	-27
4000	-17
5000	-19
6000	-12
8000	-13

Chapter 5

COMPARISON AND DISCUSSION OF MEASURED AND COMPUTED RESULTS

This chapter describes the comparisons of the experimental and the finite element results. The first step in these studies was to conduct a modal analysis in order to check the validity of the model. This was essential to conclude whether the same model could be used with confidence to calculate radiation efficiencies. Once the mesh refinement of the finite element model was accepted, the calculated mode shapes and their corresponding frequencies were compared to the experimental mode shapes and frequencies in air and in water. Then, the radiation efficiencies in water of the numerical and physical models were compared.

The modal analysis from 0 Hz to 8000 Hz was carried out and the highest order mode shapes were examined to determine the acceptability of the mesh refinement. MSC/NASTRAN recommends 8 to 10 elements per half wave for dynamic analysis. In order to be as computationally efficient for all segments of these analyses, eight elements per half wave were deemed sufficient at the highest frequencies.

The mode shapes were determined to match very well, however the numerical frequencies were too low. There were two possible approaches for increasing the frequencies of the numerical model so that they corresponded more closely to the experiments: either to remove mass by decreasing the density of the material or to add stiffness by altering the Young's modulus. Arbitrarily, the decision was made to alter the Young's modulus of the finite element model until there was very good agreement between the frequencies of both models. The actual Young's modulus of NAB is $E = 16.0 \times 10^6$ psi. The Young's modulus of the finite element model was changed to $E = 17.55 \times 10^6$ psi, which represents a 9% alteration.

The mechanical damping implemented in the finite element model for modal analysis was the experimentally determined loss factors; the loss factors were used for both the "in-air" and "in-water" modal analyses. Their values were shown previously in Table 3.3. Table 5.1 shows the comparison between the mode shapes and frequencies of the in-air and in-water modal analyses. The experimental analysis was unable to detect some of the mode shapes which were apparent in the finite element modal analysis which is due to the placement of the PZT strips. At times, it was difficult for the strips to excite some of the longitudinal bending modes because the PZT strips act in shear, not normal to the surface of the plate. Figures 5.1 to 5.4 show that the mode shapes of the two models in both water and air correspond remarkably well. If the mode shapes of

the two models had not shown good agreement, the subsequent volume velocities could not have been used to obtain reasonable values of the radiation efficiencies of the actual plate. This is due to the dependence of the radiation efficiency on the velocity of the structure as shown in equation 3.1. Because the volume velocities are determined from the net volume displacements of the structure, even small differences in the mode shapes can lead to large differences in radiation efficiency.

Table 5.1 Comparison between calculated and measured mode shapes and natural frequencies for completely free, nickel-aluminum-bronze plate.

mode shape	experimental in-air (Hz)	finite element in-air (Hz)	experimental in-water (Hz)	finite element in water (Hz)
(1,1)	664	661		583
(2,0)	697	690	597	597
(2,1)	1490	1491	1320	1333
(0,2)	1810	1811	1610	1611
(3,2)		1847		1642
(1,2)	2270	2265		2021
(3,1)	2680	2682		2428
(2,2)	3130	3173	2840	2886
(4,0)	3680	3504	3280	3300

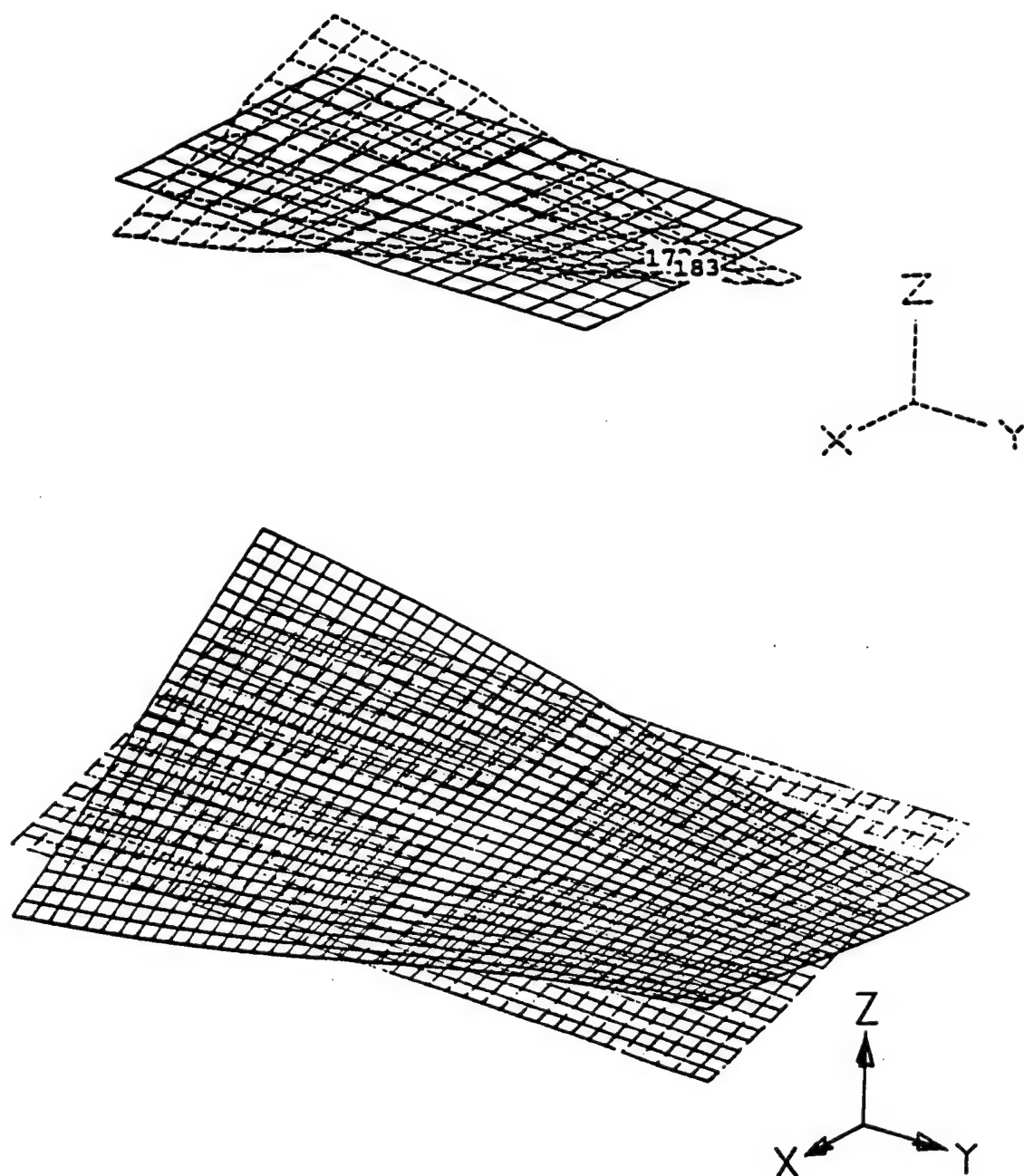
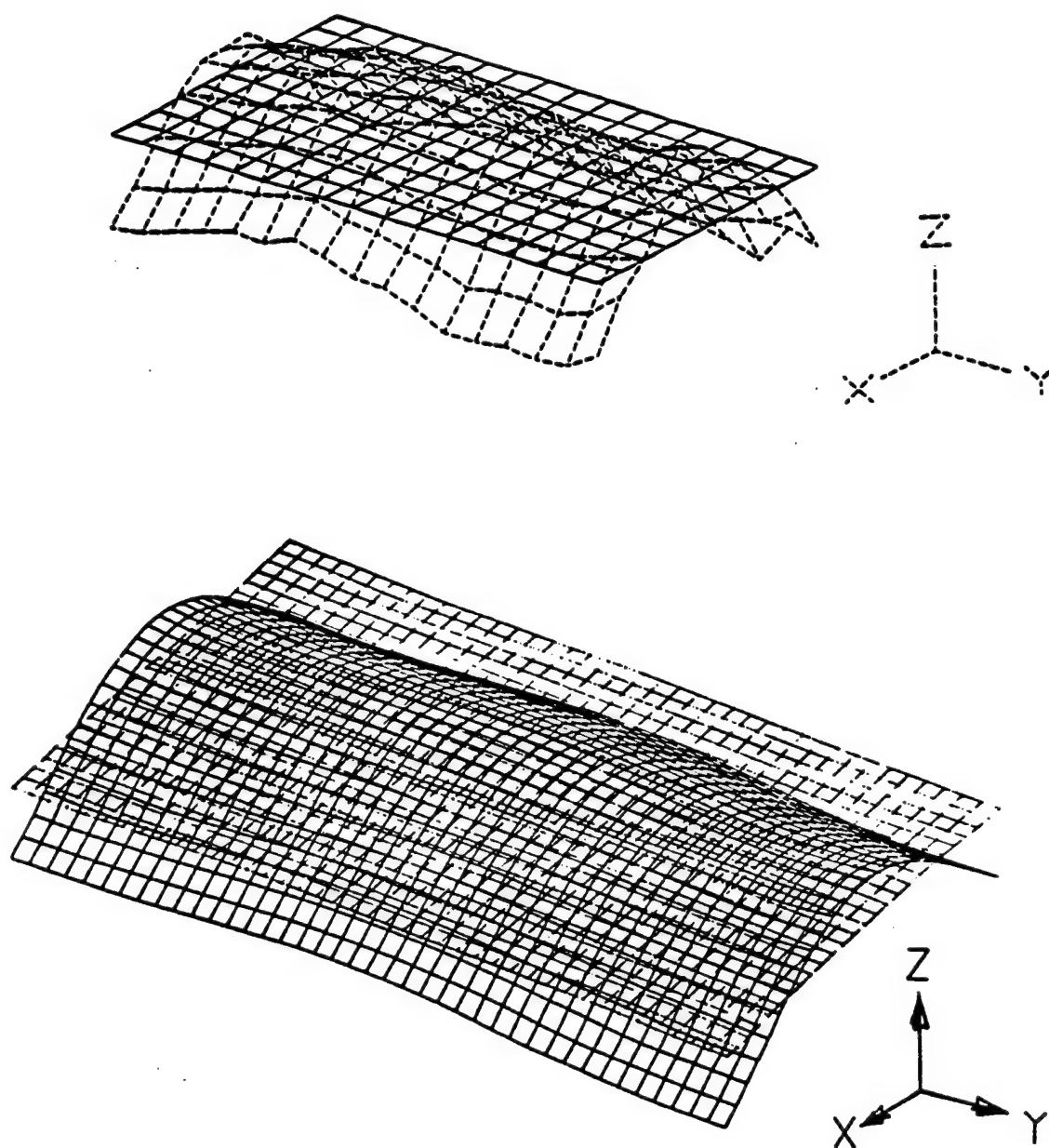


Figure 5.1 Experimental (1,1) mode, 664 Hz (top) vs.
numerical (1,1) mode, 661 Hz (bottom) in air



**Figure 5.2 Experimental (0,2) mode, 1810 Hz (top) vs.
numerical (0,2) mode, 1811 Hz (bottom) in air**

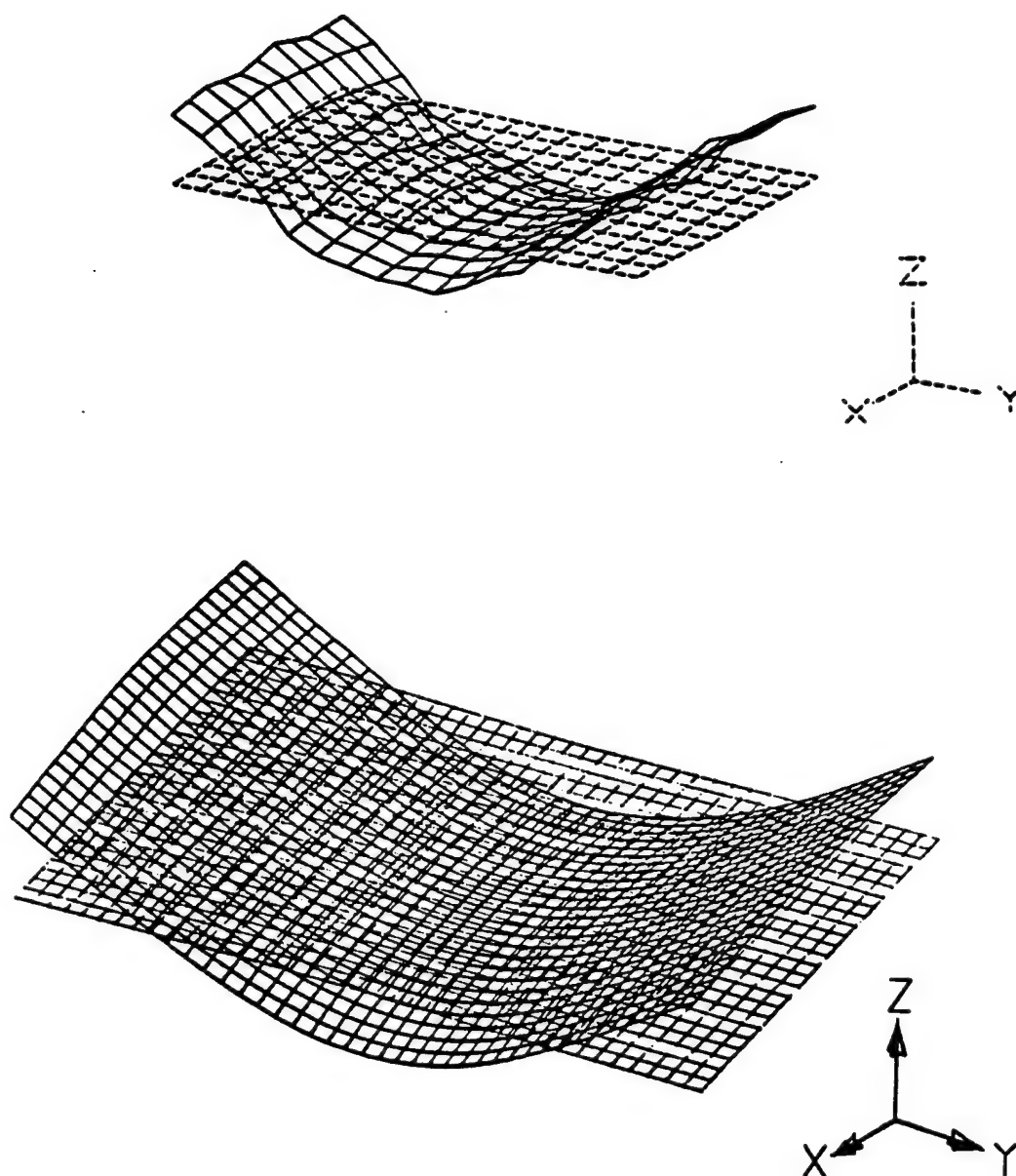


Figure 5.3 Experimental (2,0) mode, 597 Hz (top) vs. numerical (2,0) mode, 597 Hz (bottom) in water

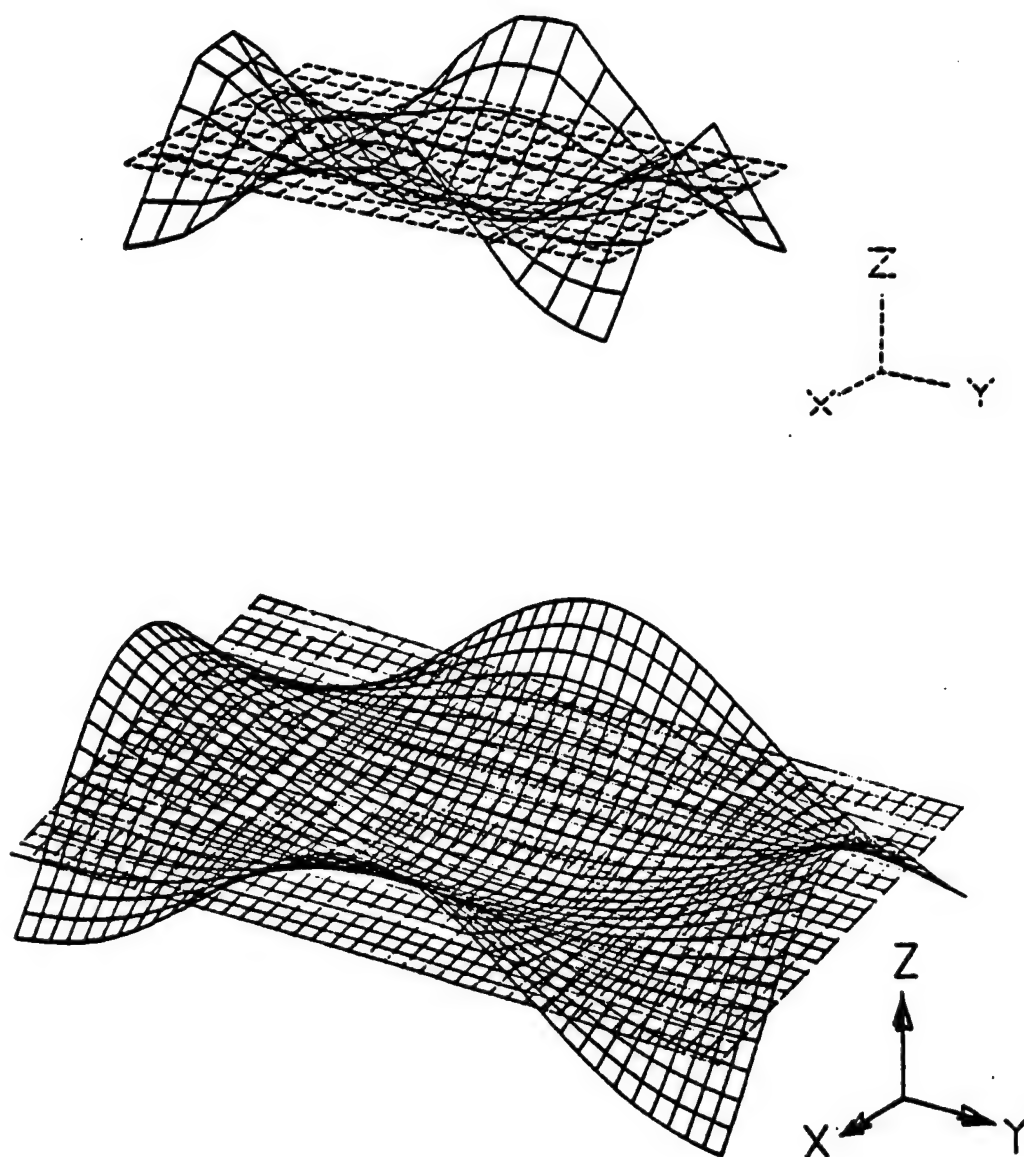


Figure 5.4 Experimental (2,2) mode, 2840 Hz (top) vs. numerical (2,2) mode, 2886 Hz (bottom) in water

Once the finite element model was determined to predict accurately the vibration responses of the physical model, as indicated by the modal analyses, a frequency response analysis was conducted to ascertain the moment excitation from the piezoelectric actuators. An iterative process was used to determine the best possible match between the transfer functions of the numerical and physical models.

First, the magnitude of the moment excitation was increased in the numerical model until the floor of the numerical transfer function reached the same level as the experimental transfer function. After a number of iterations, it was decided to divide the frequency response analysis into three separate frequency ranges as previously described in Chapter four. This is required because the moment excitation is frequency dependent. The selection of the three frequency ranges was chosen so that the floor of the transfer function matched for each frequency range .

After the determination of the moment excitation was completed, the mechanical damping was adjusted through a similar iterative process so that the amplitudes of the resonant peaks corresponded as closely as possible. Table 5.2 shows the comparison of the experimental and numerical loss factors which were used. Figure 5.5 shows a comparison between the numerically generated and experimentally generated transfer functions.

Table 5.2 Comparison between loss factors of nickel-aluminum-bronze plate submerged in water

experimental frequency (Hz)	numerical frequency (Hz)	experimental η in-water	numerical η in-water
	584		0.0
597	597	0.01	0.0
1320	1333	0.01	0.02
1610	1611	0.02	0.01
	1642		0.01
2030	2021	0.02	0.05
2420	2428	0.01	0.01
2840	2886	0.02	0.01
3280	3300	0.02	0.02
3540	3504	$\ll 1$	0.005
3890	3930	$\ll 1$	0.04

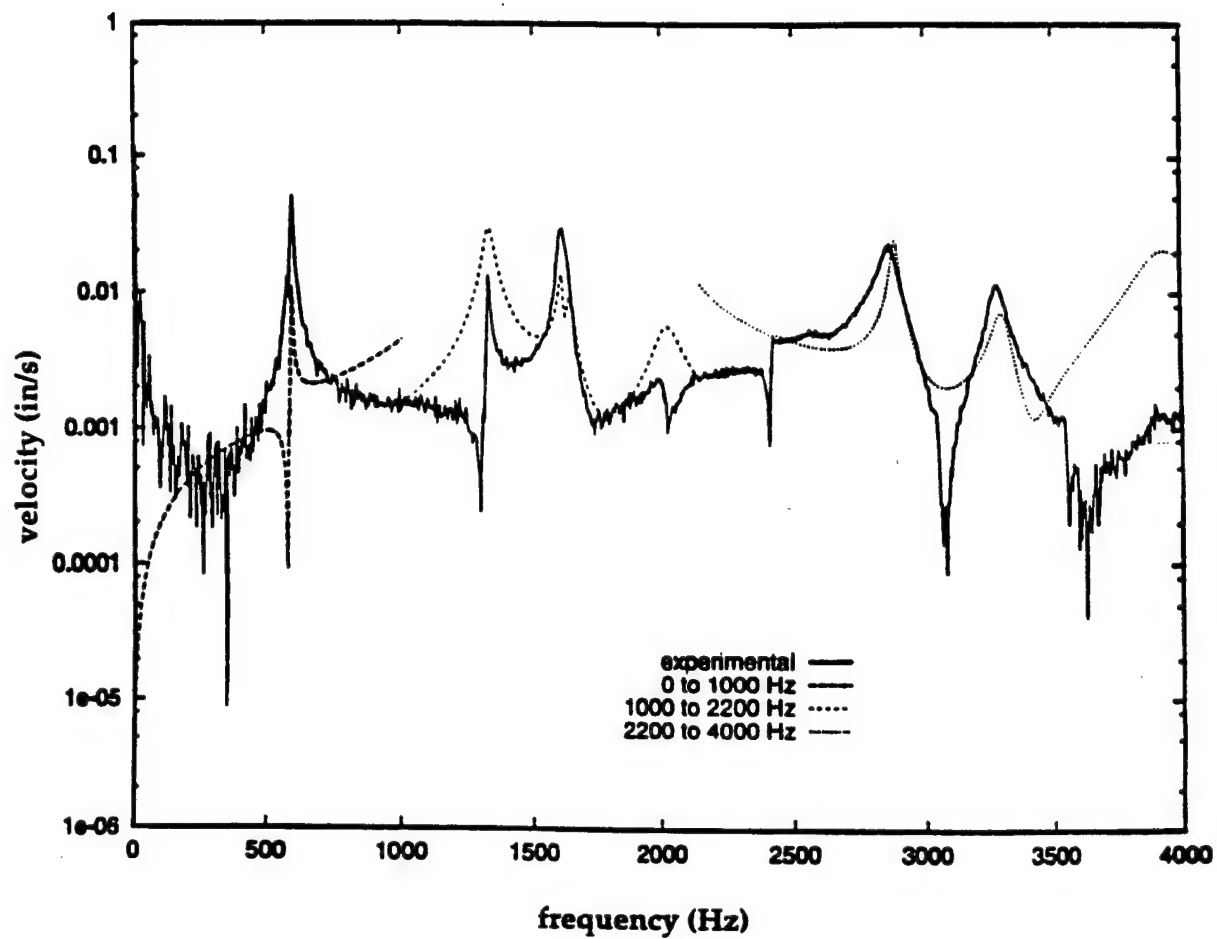


Figure 5.5 Comparison between experimental and numerical transfer functions of an un baffled, rectangular, flat plate

Neither the experimental damping nor the experimental transfer functions were measured above 4000 Hz, therefore assumptions were made for these numerical values. η was assigned a value of 0.01 for frequencies between 4000 Hz and 10000 Hz and the moment excitation was chosen to be 15 in-lb in this same frequency range. After satisfactory moments and damping were chosen, the three separate frequency response analyses were executed. The half power points of the natural frequencies were included so as not to miss the resonant peaks.

The displacements from these analyses were then used as input to the POWER code. The power output in watts was averaged for each of the eight, one third octave center frequencies before the radiation efficiency was calculated. The assumption is made that all of the sound power is dominated by the contributions from the resonance frequencies of the structure. A plot of the comparison between the experimental results and the numerically predicted radiation efficiencies is shown in Figure 5.6; their values are listed in Table 5.3.

The match in radiation efficiencies is impressive. The predictions in six of the eight one third octave frequency bands are well within acceptable ranges of experimental or numerical error (e.g. ± 3 dB). The reason for the difference in the 5000 Hz center frequency is not known. Because the experimental radiation efficiency is so much higher than all of the other values, it is possible that there was an experimental error

Table 5.3 Comparison between radiation efficiencies of an unbaffled, rectangular, flat plate submerged in water

center frequency (Hz)	experimental σ	numerical σ	Δ dB
2000	-29	-32	-3
2500	-28	-26	+2
3150	-28	-27	+1
4000	-18	-17	+1
5000	-5	-19	-14
6000	-13	-12	+1
8000	-14	-13	+1

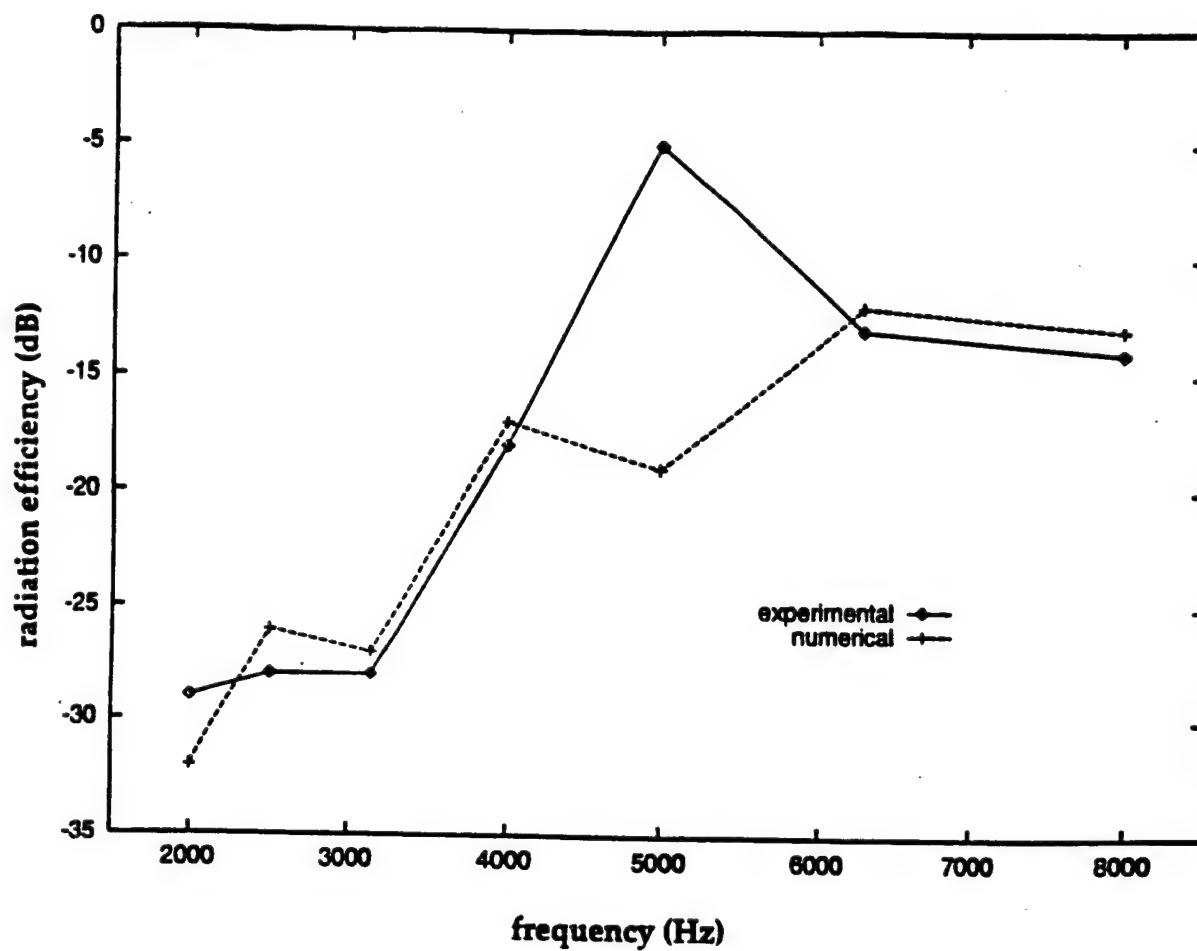


Figure 5.6 Comparison between experimental and numerical σ of an unbaffled, rectangular, flat plate submerged in water

Chapter 6

CONCLUSIONS AND RECOMMENDATIONS FOR FUTURE WORK

A method for modeling the sound power radiated by a vibrating structure has been demonstrated. The structure selected was an unbaffled, rectangular, flat plate. The results of the numerical model were compared with data collected from an actual plate excited with piezoceramic actuators. This technique employed can be summarized as follows:

1. Experimental data was generated to provide a basis for comparison of the numerically generated data. The experimental data consisted of mode shapes and their corresponding frequencies, actuator voltage/acceleration transfer functions, mechanical loss factors and one third octave radiation efficiencies.
2. Adjusted material properties and the mechanical damping from the experimental measurements were incorporated into the finite element model. The results of the modal analysis were used and adjustments were made of the material properties in the numerical model so that the resonance frequencies and mode shapes corresponded to the physical experiments.

3. A numerical frequency response analysis was executed which generated plate surface transfer functions. These transfer functions were compared with the experimentally recorded actuator voltage/acceleration levels. This method was devised to ascertain the frequency dependent moment excitation of the PZT strips.

4. Separation into three separate but contiguous frequency response analyses using the appropriate mechanical damping and moment excitations was carried out to allow the extraction of the displacements (volume velocities) at each grid point for use in the acoustic radiation program.

5. These displacements were used to calculate the radiation efficiencies of the plate. Verification was based on the comparison of these results with the experimentally determined radiation efficiencies.

This procedure can be used to predict radiated sound power for other structures made from Nickel-Aluminum-Bronze by choosing the mechanical damping and material properties to be the same as those determined in this work. It is recommended that the structures be excited by the same type of piezoceramic actuators so that the same procedure used here can be used to determine the frequency dependent moment excitations. This avoids the added mass problems inherent in the more commonly used electro-mechanical shakers.

This comparison study shows that this method for numerically computing the sound power radiated by a vibrating structure produces results that show remarkable agreement with those generated experimentally. The implementation of the method is quite straightforward and differs from previous acoustic boundary element methods in the way the boundary condition is enforced, i.e. it uses a volume velocity matching approach.

We intend to continue this work by implementing this procedure for other rectangular plates made from aluminum 7076 and stainless steel 316. The same method will be used to determine the mechanical damping and material properties to produce numerical results that correlate with the experimental data. We will measure the mechanical damping and the actuator voltage/acceleration transfer functions in the physical experiments to frequencies above 8 KHz to verify the correct moment excitation. The finite element mesh refinement will also be chosen with the intent to calculate one third octave radiation efficiencies above 8 KHz.

REFERENCES

1. Atalla, N., J. Nicolas and C. Gauthier, "Acoustic Radiation of an Unbaffled Vibrating Plate with General Elastic Boudary Conditions", J. Acoust. Soc. Am., 99(3), March 1996.
2. Beranek, L. L., *Noise and Vibration Control*, (Institute of Noise Control Engineering, 1988).
3. Blake, W. K., "The Radiation from Free-Free Beams in Air and Water", J. Sound and Vibration, 33(4), pp.427-450 (1974).
4. Capone, D. E., personal communication.
5. Cook, R. D., D. S. Malkus and M. E. Plesha, *Concepts and Applications of Finite Element Analysis*, (John Wiley and Sons, 1989).
6. Crawley, E. F., and J. D. Luis, "Use of Piezoelectric Actuators as Elements of Intelligent Structures", AIAA Journal, Vol. 25, No. 10, October 1987, pp.1373-1385.
7. Cremer, L., M. Heckl, and E. E. Ungar, *Structure-Borne Sound*, (Springer-Verlag, 1973).
8. Erickson, M. E., personal communication.
9. Fahnline, J. B. and G.H. Koopmann, "Numerical Implementation of the Lumped Parameter Model for the Acoustic Power Output from a Vibrating Structure", J. Acoust. Soc. Am., to be published.
10. Fahy, F., *Sound and Structural Vibration*, (Academic Press, 1985).
11. Gorman, D. J. and R. K. Sharma, "A Comprehensive Approach to the Free Vibration Analysis of Rectangular Plates by use of the Method of Superposition", J. Sound and Vibration, V47, 1976.

12. Harbold, T. L., "Numerical Predictions of Acoustic Radiation by Unbaffled Finite Plates Using Non-intrusive Velocity Measurements "Master's Thesis, The Pennsylvania State University, 1993.
13. Kinsler, L. E. and A. R. Frey, *Fundamentals of Acoustics*, (John-Wiley and Sons, 1982).
14. Koopmann, G. H. and J. B. Fahrlne, *Designing Quiet Structures: A Sound Power Minimization Approach*, (Center for Acoustics and Vibrations, The Pennsylvania State University, University Park, PA, 1996).
15. Koopmann, G. H., L. Song and J. B. Fahrlne, "A Method for Computing Acoustic Fields Based on the Principle of Wave Superposition", J. Acoust. Soc. Am., vol. 86 No. 6, December 1989.
16. LABVIEW, *Data Acquisition VI*, (National Instruments Corporation, 1992).
17. McFarland, D., B. L. Smith and W. D. Bernhart, *Analysis of Plates*, (Spartan Books, 1972).
18. MSC/NASTRAN, *Handbook for Dynamic Analysis*, (The MacNeal-Schwendler Corporation, 1983).
19. MSC/NASTRAN, *Quick Reference Guide*, (The MacNeal-Schwendler Corporation, 1983).
20. MSC/XL, *User's Manual V3B*, (The MacNeal-Schwendler Corporation, 1993).
21. Star Modal, *The STAR System User's Manual*, (GenRad Inc., 1994).
22. St. Pierre, R. L., "Minimization of Radiated Sound Power from Beams and Plates Using Distributed Point Masses", Master's Thesis, The Pennsylvania State University, 1993.
23. Weyer, R. M. and R. P. Szwerc, "The Damping Efficiency of Metal and Composite Panels", Second International Congress on Recent Developments in Air- and Structure-Borne Sound and Vibration, (March 4-6, 1992).
24. Williams, E. G., "Numerical Evaluation of the Radiation from Unbaffled , Finite Plates Using the FFT", J. Acoust. Soc. Am., 74(1), July 1983.

25. Williams, E. G., and J. D. Maynard, "Numerical Evaluation of the Rayleigh Integral for Planar Radiators Using the FFT", J. Acoust. Soc. Am., 72(6), December 1982.
26. Zienkiewicz, O. C., *The Finite Element Method*, (England, McGraw Hill, 1977).